Technical Design Report on the E80 Experiment:

Systematic investigation of the light kaonic nuclei
(2024 revised version)

submitted on May 30, 2024
(updated on July 5, 2024)

K. Itahashi, M. Iwasaki, T. Hashimoto, Y. Ma, R. Murayama, T. Nanamura,
F. Sakuma[*]

RIKEN, Saitama, 351-0198, Japan

T. Akaishi, K. Inoue, S. Kawasaki, T. Nagae, H. Noumi, K. Shirotori

Research Center for Nuclear Physics (RCNP), Osaka University, Osaka, 567-0047, Japan

Y. Kimura, G. Kojima, H. Ohnishi, K. Toho, M. Tsuruta

*Research Center for Accelerator and Radioisotope Science (RARIS), Tohoku University,
Sendai, 982-0826, Japan*

M. Iio, S. Ishimoto, Y. Makida, H. Ohhata, M. Oonaka, K. Ozawa, K. Sasaki,
N. Sumi, S. Suzuki, T. Yamaga, M. Yoshida

High Energy Accelerator Research Organization (KEK), Ibaraki, 305-0801, Japan

K. Tanida

Japan Atomic Energy Agency (JAEA), Ibaraki 319-1195, Japan

H. Fujioka

Department of Physics, Tokyo Institute of Technology, Tokyo, 152-8551, Japan

S. Okada

Chubu University, Aichi, 487-0027, Japan

M. Bazzi, A. Clozza, C. Curceanu, C. Guaraldo, M. Iliescu, S. Manti, A. Scordo,
F. Sgaramella, D. Sirghi, F. Sirghi

Laboratori Nazionali di Frascati dell' INFN, I-00044 Frascati, Italy

P. Buehler, E. Widmann, J. Zmeskal

Stefan-Meyer-Institut für subatomare Physik, A-1090 Vienna, Austria

---

[*]Spokesperson, E-mail: sakuma@ribf.riken.jp

Abstract

In this document we report on the technical design of the J-PARC E80 experiment. The E80 experiment aims at the precise measurement of kaon-nucleus bound systems (kaonic nuclei), focusing on the $\bar{K}NNN$ ($A = 3$) system as a first step towards a comprehensive study of the light kaonic nuclei from "$\bar{K}N$" ($=\Lambda(1405)$) to "$\bar{K}NNNN$". Through the experiments and detailed theoretical calculations, we will unravel the nature of the kaonic nuclei from the property changes depending on the mass number A. To achieve the systematic measurements, we are now constructing a new 4π Cylindrical Detector System (CDS) to drastically increase the acceptance. We have also proposed to improve the K1.8BR beam line by shortening it to utilize the more intense K^- beam.

Contents

1 Introduction

The study of the $\bar{K}N$ interaction is one of the most important subjects to understand meson-baryon interactions in low-energy quantum chromodynamics (QCD). Extensive measurements of the anti-kaonic hydrogen atom [1–3] and low-energy $\bar{K}N$ scattering [4] have revealed the strongly attractive nature of the $\bar{K}N$ interaction in the isospin I = 0 channel. Consequently, the possible existence of deeply bound kaonic nuclear states (kaonic nuclei) has been widely discussed [5–24]. Theoretical calculations indicate that kaonic nuclei can form compact systems, suggesting that high-density nuclear matter is realized in kaonic nuclei where chiral symmetry is expected to be restored.

Among the kaonic nuclei, the $\bar{K}NN$ system with $I = 1/2$ and $J^P = 0^-$ (symbolically denoted as K^-pp for the $I_z = +1/2$ state) is of special interest because it is the lightest $S = -1$ $\bar{K}$ nucleus and its existence is supported by many theoretical works. Despite considerable experimental efforts over the past 20 years, it has been challenging to prove the existence of K^-pp. Several groups have reported observations of a K^-pp candidate with a binding energy around 100 MeV in experiments measuring non-mesonic decay branches of Λp and/or $\Sigma^0 p$ in different reactions [25–27]. However, there are also contradicting reports concluding that the reactions can be understood without a bound state [28–31].

Recently, we confirmed the existence of the K^-pp bound state using the simplest reaction of in-flight $^3\mathrm{He}(K^-, N)$ at the J-PARC E15 experiment [32–35]. A distinct peak structure well below the mass threshold of $K^- + p + p$ was observed in the Λp invariant-mass (IM) spectrum obtained from the $^3\mathrm{He}(K^-, \Lambda p)n$ measurement as shown in Fig. 1. The simplest and most natural interpretation of this peak is K^-pp.

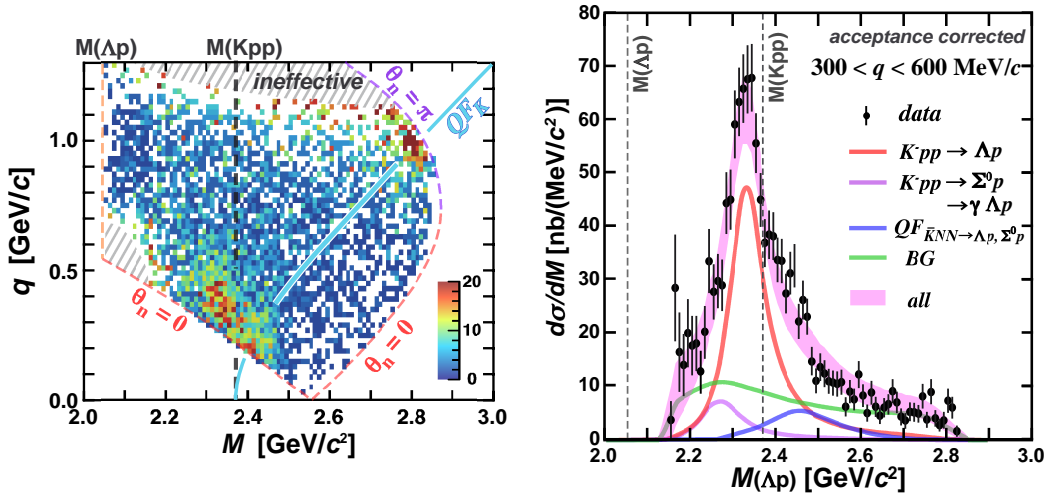
Figure 1: (left) Efficiency and acceptance corrected data over M (Λp invariant mass) and q (momentum transfer) obtained from the J-PARC E15 experiment [34,35]. (right) Λp invariant mass in the region $0.3 < q < 0.6$ MeV/c.

The result obtained in the E15 experiment is experimentally solid compared to the other experiments because we measured a wide range of momentum transfer with high statistics. However, the detailed properties need to be clarified by further experimental studies. For this purpose, we have planned a series of experimental programs using the $(K^-, N/d)$ reactions on light nuclear targets at the K1.8BR beam line. A detailed and systematic study of a range of nuclei from $\bar{K}N$ ($\Lambda(1405)$) to $\bar{K}NNNN$ will be performed using the world's highest intensity low-momentum kaon beam available at J-PARC:

- **[$\bar{\mathbf{K}}\mathbf{N}(\mathbf{\Lambda(1405)})$]** Precise measurement of the $\Lambda(1405)$ state in the large momentum transfer region via the $d(K^-, n)$ reaction to clarify experimentally whether it is a baryonic or a $\bar{K}N$ molecular state,

- **[$\bar{\mathbf{K}}\mathbf{N}\mathbf{N}$]** Investigation of the spin and parity of the $\bar{K}NN$ state via the ${}^3\text{He}(K^-, N)$ reactions,

- **[$\bar{\mathbf{K}}\mathbf{N}\mathbf{N}\mathbf{N}$]** Precise measurement of the $\bar{K}NNN$ states via the ${}^4\text{He}(K^-, N)$ reactions as a bridge to heavier systems, and,

- **[$\bar{\mathbf{K}}\mathbf{N}\mathbf{N}\mathbf{N}\mathbf{N}$]** Advanced search for the $\bar{K}NNNN$ states via the ${}^6\text{Li}(K^-, d)$ reaction.

In the series of experimental programs, we aim to determine the mass-number dependence of the binding energy, the decay width, and the decay branching ratio. Furthermore, we aim to elucidate the internal structure of kaonic nuclei, including their spatial size, by systematically and multidimensionally comparing structure and reaction calculations based on detailed theoretical models with results obtained from the experiments. The mass-number dependence has been calculated with several theoretical models, as summarized in Fig. 2. The calculated values of the binding energy and the decay width vary widely due to the differences in the $\bar{K}N$ interaction models, but almost all calculations show that the larger nuclei have stronger binding energies. For the width, the mass-number dependence does not appear to be as large as for the binding energy, in which the calculations take into account only mesonic decay channels such as $\pi\Sigma N$ and $\pi\Lambda N$. The calculated width is expected to be larger when the models include non-mesonic decay channels, as demonstrated in Ref. [17].

In parallel to these studies, we also intend to access the $S = -2$ kaonic nuclei, such as the theoretically predicted K^-K^-pp state. The $S = -2$ system could allow us to access even higher density systems than the $S = -1$ kaonic nuclei. As described in our Letter of Intent [36], a possible approach for the measurements at J-PARC could be:

- **[$\bar{\mathbf{K}}\bar{\mathbf{K}}\mathbf{N}\mathbf{N}$]** Search for $\bar{K}\bar{K}NN$ states via $\bar{p}{}^3\text{He}$ annihilation.

To ensure that the measurements are systematic and precise, we are constructing a new 4π spectrometer to measure all the particles involved in the reactions and to reconstruct exclusively the formation and decay of kaonic nuclei. The spectrometer is
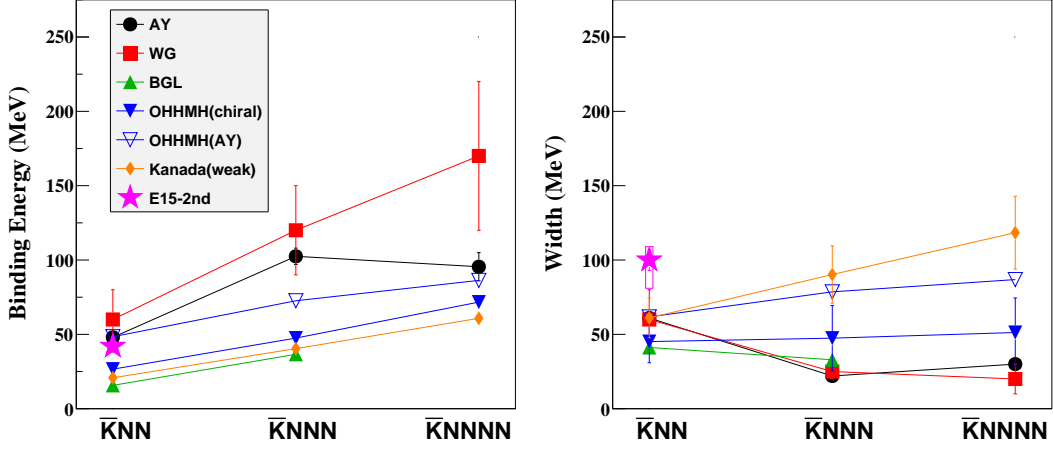
Figure 2: Summary of theoretical calculations of kaonic nuclei from $A = 2$ to 4 in different models AY [6, 7], WG [13], BGL [16], OHHMH [22], and Kanada [37]. The result obtained from the E15 experiment is also plotted [35].

designed to be highly versatile so that all the experiments can be performed by simply changing the target materials. In addition, for more efficient use of the high-intensity kaon beam, we have proposed to shorten the existing K1.8BR beam line to increase the kaon yield without deteriorating the momentum resolution of the kaon beam.

In this document we describe the technical details of the new spectrometer to conduct an experimental study of the $\bar{K}NNN$ bound state as a first step towards the systematic investigation of light kaonic nuclei.

2 J-PARC E80 Experiment

We aim to measure the $\bar{K}NNN$ ($A = 3$) system as a first step towards a comprehensive study of kaonic nuclei. E80 provides for the first time the mass-number dependence of kaonic nuclei by combining the obtained properties of the $\bar{K}NNN$ state with those of the previously reported K^-p ($\Lambda(1405)$) and K^-pp states. The dependence can reveal the $\bar{K}N$ interaction below the mass threshold and the internal structure of kaonic nuclei with the help of detailed theoretical calculations.
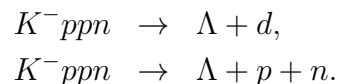
2.1 Experimental Method

The key to the experimental search is to adopt a simple reaction and measure it exclusively. The adoption of a simple reaction, such as in-flight $\bar{K}$ induced reactions with light target nuclei, enables us to specify the reaction channel by minimizing the contribution of reactions unrelated to kaonic nucleus formation. Exclusive measurements are crucial to distinguish small and broad signals from the large and widely distributed quasi-free and multi-nucleon absorption backgrounds. From the experience of E15, we have learned that reducing the number of particles in the final state is a key to removing ambiguities in the interpretation of the reaction process.Therefore, we focus on the $\bar{K}NNN$ system with $I = 0$ and $J^P = 1/2^-$ (symbolically denoted as K^-ppn) with its Λd and Λpn decay channels in $^4\mathrm{He}(K^-, \Lambda d/\Lambda pn)n$ reactions.

In the E80 experiment, we perform exclusive measurements of the production and decay of the K^-ppn state using the in-flight reaction

$$K^- + {}^4\mathrm{He} \quad \rightarrow \quad K^-ppn + n$$
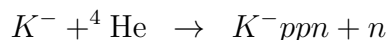
followed by the expected non-mesonic decays

$$
\begin{aligned}
K^-ppn &\rightarrow \Lambda + d, \\
K^-ppn &\rightarrow \Lambda + p + n.
\end{aligned}
$$

To maximize the $(\bar{K}, N)$ reaction rate around zero degrees, as shown in Fig 3, we utilize 1.0 GeV/c incident kaons. We determine the binding energy and decay width from the invariant mass reconstruction of the decays. The invariant mass must be obtained in the wide momentum transfer region in order to distinguish the bound state production from the quasi-free processes by the event kinematics, as demonstrated in the E15 analysis.
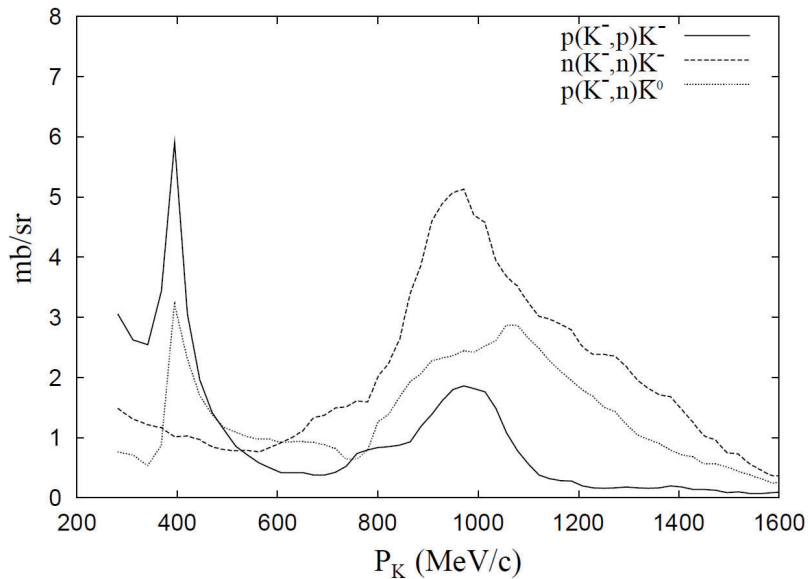
Figure 3: Cross sections of the $K^- N \rightarrow \bar{K} N'$ reactions at $\theta_n = 0°$ (nucleon forward / kaon backward) [38].

2.2 Apparatus

The E80 experiment is conducted in the K1.8BR area of the Hadron Experimental Facility. The incoming K^- beam momentum is analyzed by the beam line spectrometer. The beam kaon then collides with a liquid ^{4}He target located at the final focus point, and particles produced from the reactions are measured with a Cylindrical Detector System (CDS) surrounding the target system. A forward or backward going particle out of the CDS acceptances is identified using the missing mass technique, allowing all particles from the reactions to be identified. A design of the CDS is shown in Fig. 4. It consists mainly of a large superconducting solenoid magnet, a Cylindrical wire Drift Chamber (CDC), and a Cylindrical Neutron Counter (CNC). The details of each apparatus used for the experiment are described starting in Sec. 4.
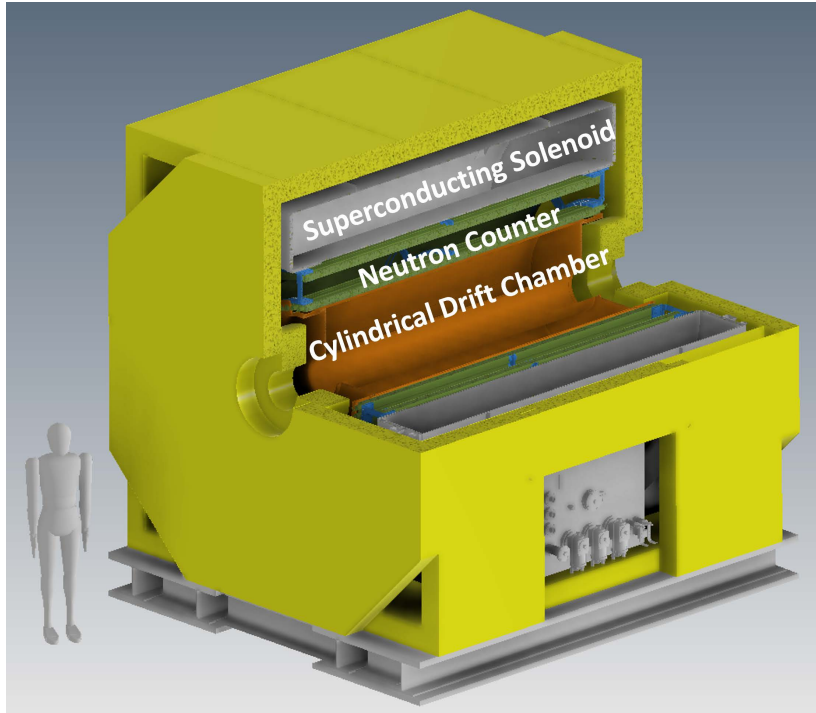
Figure 4: Design of the CDS.

2.3   Expected Yield

Recently, we analyzed the Λdn final state of the K^{-4}He reaction at 1 GeV/c using the T77 data and found a kinematic anomaly below the mass threshold of $M(K^- ppn)$ with a structure similar to that of the Λpn final state of the K^{-3}He reaction [39]. As in the case of the $\bar{K}NN$ bound state in the Λpn final state, the observed structure in the Λdn final state would be the signal of the $K^- ppn$ bound state. The cross section of the peak structure has been preliminary evaluated to be $\sim 5\ \mu$b, which is smaller than the initial estimate in the E80 proposal. To estimate the expected yield of the $K^- ppn$, we use this preliminary cross section for the $K^- ppn \rightarrow \Lambda d$ decay, and we assume that the $K^- ppn \rightarrow \Lambda pn$ branching ratio is the same as the Λd decay, $i.e.$,

$$
\begin{aligned}
\sigma^{tot}_{Kppn} \cdot BR(\Lambda d) &\sim 5\ \mu\text{b}, \\
\sigma^{tot}_{Kppn} \cdot BR(\Lambda pn) &\sim 5\ \mu\text{b}.
\end{aligned}
$$

The detector acceptance of the CDS (Ω_{CDS}) is evaluated with a full detector simulation using the GEANT4 toolkit ver.10.2.3 with the "QGSP_BERT_HP" physics list [40].

The estimated yields for each channel, normalized to 1 G (10^9) K^- beam at the trigger level, are summarized in Table 1. The CDS acceptance of Ω_{CDS} is obtained for the exclusive reconstruction of ^{4}He$(K^-, \Lambda d/\Lambda pn)n$. The yields are calculated using

the following equation:

$$N = \sigma \times N_{beam} \times N_{target} \times \epsilon,$$
$$\epsilon = \epsilon_{DAQ} \times \epsilon_{trigger} \times \epsilon_{beam} \times \epsilon_{fiducial} \times \Omega_{CDS} \times \epsilon_{CDS},$$

where

N : expected yield,

σ : cross section including the decay branching ratio,

N_{beam} : number of the beam kaons,

N_{target} : number of the target particles,

ϵ : total experimental efficiency,

ϵ_{DAQ} : DAQ efficiency,

$\epsilon_{trigger}$: trigger efficiency,

ϵ_{beam} : analysis efficiency of the beam kaons,

$\epsilon_{fiducial}$: efficiency of fiducial volume selection,

Ω_{CDS} : detector acceptance of the CDS,

ϵ_{CDS} : analysis efficiency of the CDS.

Table 1: Estimated yield of the K^-ppn bound state normalized to 1 G (10^9) K^- beam at trigger level.

decay mode	Λd	Λpn
$\sigma^{tot} \cdot BR$	assumed to be 5 μb	
N_{beam}	10^9	
N_{target}	2.56×10^{23}	
ϵ_{DAQ}	0.92	
$\epsilon_{trigger}$	0.98	
ϵ_{beam}	0.72	
$\epsilon_{fiducial}$	0.65	
Ω_{CDS}	0.23	0.047
ϵ_{CDS}	0.6	0.3
N	80	8

The calculation of N_{target} uses the fiducial volume length of 11.8 cm for the T77 analysis. Ω_{CDS} for the Λpn channel is evaluated with a plastic scintillation counter equivalent to the 12cm thick CNC, where the neutron detection efficiency is obtained

to be in the range of $\sim 12\%$ (at ~ 1.0 GeV/c) to $\sim 36\%$ (at ~ 0.2 GeV/c) from the Geant4 simulation. We assume the same parameters obtained and evaluated in the analysis of the predecessor experiments at the K1.8BR: $\epsilon_{DAQ} = 0.92$, $\epsilon_{trigger} = 0.98$, $\epsilon_{beam} = 0.72$, and $\epsilon_{fiducial} = 0.65$. The analysis efficiencies of the CDS, $\epsilon_{CDS} = 0.6$ for the Λd channel and $\epsilon_{CDS} = 0.3$ for the Λpn channel, are assumed based on the result of $K^-{}^3\mathrm{He} \to \Lambda pn$ analysis [35] and that of $K^-{}^3\mathrm{He} \to \pi\Sigma pn$ analysis [41], respectively.

On the improved K1.8BR beam line, we expect 2.5×10^5 kaons on target per spill at a momentum of 1.0 GeV/c, under the MR beam power of 90 kW with 4.2 repetition cycles. Table 2 shows the estimated yields at 3 weeks beam time, assuming 90% accelerator uptime: 100 G kaons on target (155 G beam kaon at kaon trigger level without fiducial volume selection).

Table 2: Estimated K^-ppn yield for a three-week data taking using the 90 kW MR beam power.

decay mode	Λd	Λpn
$\sigma^{tot} \cdot BR$	assumed to be 5 μb	
accelerator up-time	0.9	
# of K^- beam	155×10^9	
# of K^- on target	100×10^9	
# of expected yield	1.2×10^4	1.2×10^3

2.4 Cost and Schedule

The construction of the E80 spectrometer has been started from FY2022 with a research grant "Grant-In-Aid for Specially Promoted Research by JSPS (FY2022-26)". The preparation of the superconducting (SC) solenoid magnet and the CDC is fully covered by this grant, and their construction and commissioning are underway. The construction cost of the CNC is covered by another grant from JSPS "Grant-in-Aid for Scientific Research (S) (FY2024-28)", which we recently received. Other apparatus required for the E80 experiment is the same as that used in the current K1.8BR: beam line counters and chambers, a liquid $H_2/D_2/{}^{3,4}\mathrm{He}$ target system, and a vertex fiber tracker.

As for the K1.8BR area upgrade, we are now working on a realistic design of the K1.8BR area configuration, including a future test beam line to be constructed next to K1.8BR, with shielding calculation using the MARS code in close cooperation with the HD-BL group. Cost estimation is also underway, with the hope that the cost of the upgrade will be covered by a facility budget.

The E80 preparation schedule is shown in Fig. 5, and below are summaries for each preparation.

	FY2022				FY2023				FY2024				FY2025				FY2026				FY2027			
	Q1	Q2	Q3	Q4	Q1	Q2	Q3	Q4	Q1	Q2	Q3	Q4	Q1	Q2	Q3	Q4	Q1	Q2	Q3	Q4	Q1	Q2	Q3	Q4
SC Solenoid Magnet	Design		Purchase (SC Wire)		Construction										Stored at KEK		Install ation	Integration, Test & Commissioning			Commissioning w/ Beam	Physics Run	Analysis & Pblication	
CDC	Design					Construction			Test & Commissioning															
NC	Design & R&D										Purchase (Scinti.)	Asse mbly	Test & Commissioning											
K1.8BR Beam Line	E73(CDS) -> E72(HypTPC) Experiments															Upgrade	E80 Experiment							

Figure 5: E80 preparation schedule.

- **Supserconducting Solenoid Magnet** The design was completed in the first half of FY2022, and the superconducting wire was purchased in the last half of FY2022. A return yoke was also constructed in FY2022 and is now stored at the KEK Tuskuba campus. In FY2023, a cold mass was constructed using the purchased superconducting wire, and in FY2024, the construction of a vacuum vessel and magnet assembly will be completed, including excitation testing without the return yoke in a production factory. After being stored at the KEK Tsukuba campus due to limited storage space at the J-PARC side, the entire assembly will be performed at the K1.8BR area in early FY2026 after the reassembly of the K1.8BR area is partially completed. The magnetic field measurement will then be performed before the CDC and CNC are installed.

- **Cylindircal Drift Chamber (CDC)** The design was completed in FY2022 using the same wire configuration as the existing CDC, but with three times the wire length. Construction began in the last half of FY2023 and will be completed in early FY2024. Commissioning at J-PARC will then begin in early FY2024.

- **Cylindrical Neutron Counter (CNC)** We are now conducting R&D studies to achieve a timing resolution of less than 100 ps with a 3 m long plastic scintillator slab with a fine-mesh PMT and MPPC readout. The design will be finalized in the first half of FY2024, and we will purchase the scintillator in the last half of FY2024. Assembly and subsequent commissioning with cosmic rays will take place in FY2025.

- **K1.8BR Beam Line** On the K1.8BR beam line, the E73 experiment will run with the existing CDS until the end of 2024. After the completion of E73, the Hyp-TPC spectrometer will be installed by replacing the existing CDS for the E72 experiment. E72 will be completed in mid FY2025. The K1.8BR upgrade will then begin and will take half a year to shorten and reassemble the beam line, followed by the installation of the CDS.

Thus, the integration and commissioning of the CDS will be completed in FY2026, after which the E80 experiment will be ready. We expect that the Stage II approval

will lead to follow-on funding and foster collaborations, especially with young Ph.D. students and full-time postdocs.

3 K1.8BR Beam Line

The E80 experiment is conducted at the K1.8BR beam line. To achieve an efficient utilization of the K^- beam at E80, we have proposed a new configuration of the beam line as shown in Fig. 6. With this new setup, the available number of kaons at 1 GeV/c is expected to increase by a factor of ~ 1.4 compared to the current beam line configuration, without deteriorating the momentum resolution of the kaon beam.
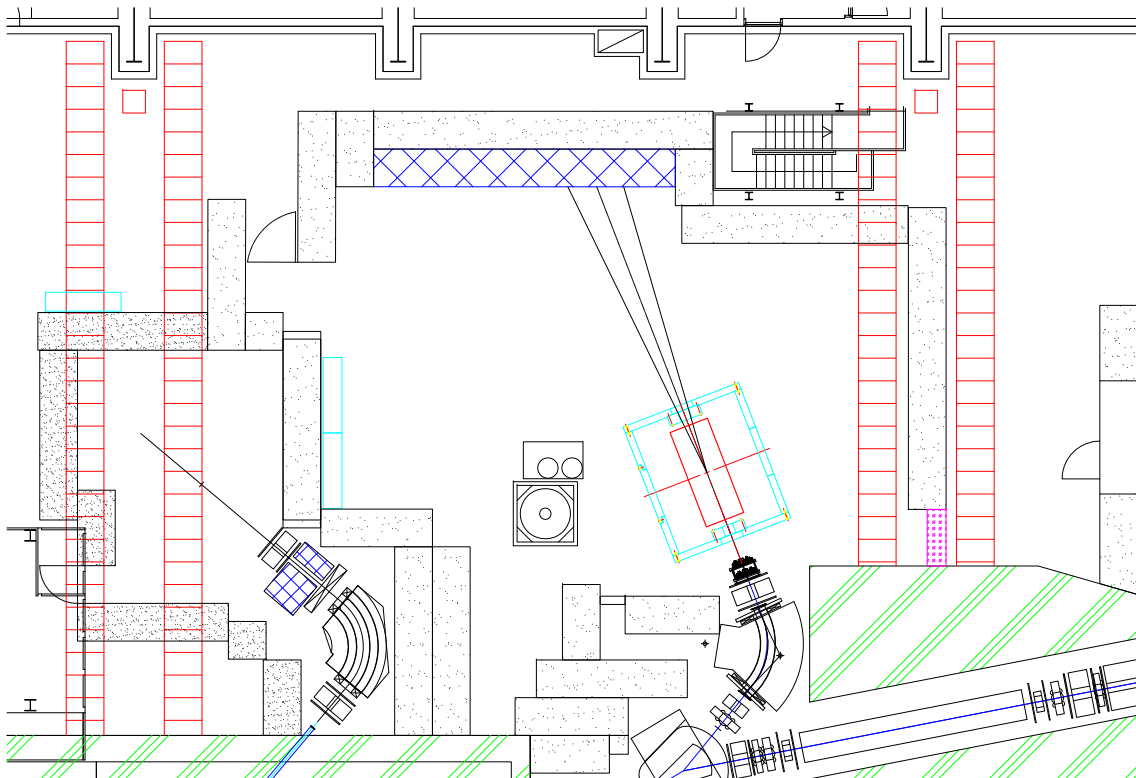
Figure 6: New layout of the K1.8BR experimental area for the E80 experiment with the future test beam line.

3.1 Beam Line Design

In the improvement, we have proposed to remove the D5 magnet to maximize the available kaon yield. Since the beam trajectory is drastically changed by the removal, it is necessary to move the beam dump along the beam direction. Therefore, we have requested to rearrange the K1.8BR experimental area as shown in Fig. 6. In the modified experimental area, the beam dump will be moved from the west side of the currently installed hadron hall to the north side. The experimental area must also be large enough to install the large CDS along the beam axis.

This modification shortens the beam line length by ~ 2.5 m. As summarized in Table 3, the beamline length is shortened by ~ 3.7 m with the removal of D5 in the original beamline design, but the final focal point is shifted downstream of the beamline by ~ 1.2 m because the size of the new CDS becomes larger than the currently used CDS as described in section. 6. The evaluated beam optics with the new beam line setup is shown in Fig. 7. In the new optics, the beam focus is expected to be almost the same size as the current beam line configuration (Fig. 8). Thus, the available kaons on target are conservatively estimated to increase by a factor of ~ 1.4, which corresponds to 2.5×10^5 kaons on target per spill at the 90 kW beam power with a 4.2 s repetition cycle [†]. In other words, comparing the new CDS on the upgraded beam line with the new CDS on the current beam line, the beam intensity increases by a factor of 1.6 (=1.4/0.9).

Table 3: Relative beam line length and beam yield compared to the current configuration with the D5 magnet.

Relative beam line length (relative beam yield)	with D5	without D5
Current CDS	0 m ($\times 1.0$)	-3.7 m ($\times 1.6$)
New CDS	+1.2 m ($\times 0.9$)	-2.5 m ($\times 1.4$)

3.2 Shielding Calculation

To evaluate the radiation level outside the experimental area, we performed a shielding calculation using the MARS code with a realistic K1.8BR design. In the new area configuration, the beam dump is located near the catwalk at the ground level and the stairway connecting the ground level and the floor level. In addition, in the southeastern part of the experimental area, there will be a gap of about 1 m in the concrete shield due to the power cables already installed. It is required that the dose in these areas be sufficiently low.

Figure 9 shows the calculated results. In the calculation, 5.0×10^6 1 GeV/c pions per second (corresponding to the current operational limit of 1.8×10^{10} pions per hour at the K1.8BR) are exposed from the center of the D4 magnet to the beam dump with the calculated beam optics and the pencil for comparison. Here the results include the safety factor of four, $i.e.$, the calculation results are multiplied by four. As shown in the figure, the radiation level is well below the 25 μSv/h limit at all points outside the experimental area, even in areas of concern such as the catwalk, stairs, and southeast gap.

[†]2.5×10^5 (Run91, 2024 @ 81 kW, 4.2 s) $\times 0.65$ (fiducial volume selection) $\times 1.4$ (beam line length) $\times 90/81$ (beam power) $\sim 2.5 \times 10^5$ (@ 90 kW, 4.2 s).
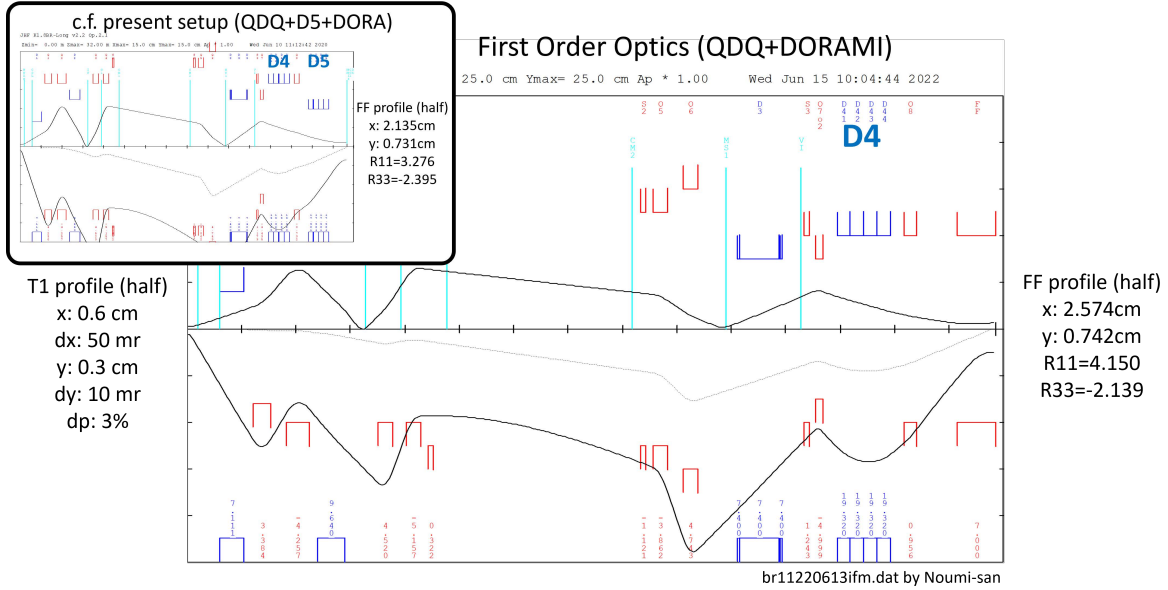
Figure 7: Beam line optics of the improved K1.8BR beam line with the first order calculation.
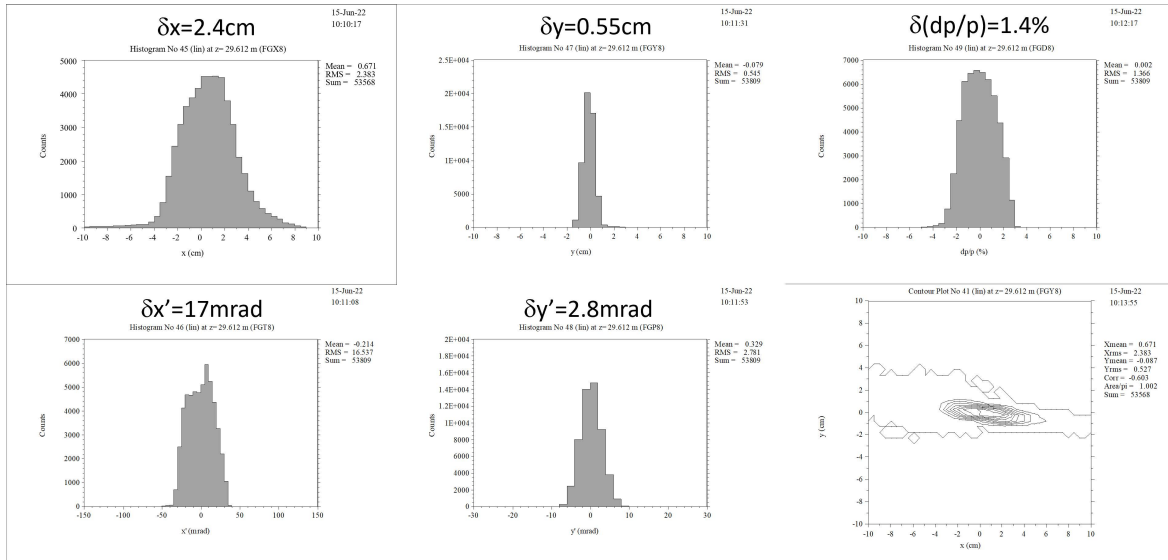
Figure 8: Beam focus at the final focus point with the third order calculation.

At the beam height (150~250 cm sliced)

Prompt dose equivalent, total (n,photon,p,,,)

Catwalk position, east-west dependence

Stair position, up-down dependence

Unit: mSv/hr

- Calculated optics
- Calculated optics (δy' x 3)
- pencil beam from D4
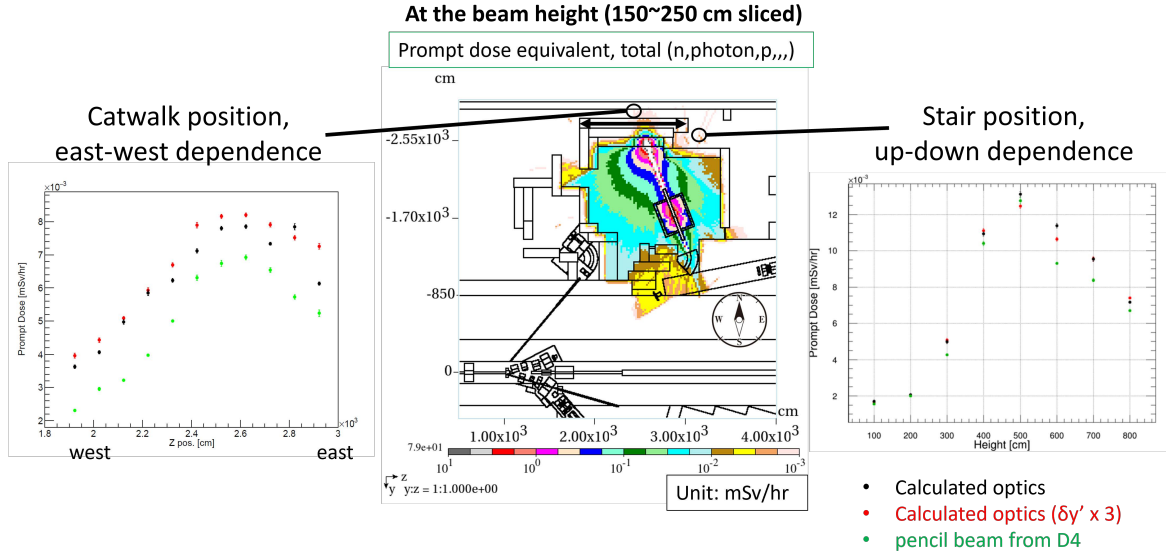
Figure 9: Shielding calculation of the modified K1.8BR area using the MARS code. Results are shown for the case that 5.0×10^6 1 GeV/c pions per second (corresponding to the current operational limit of 1.8×10^{10} pions per hour at the K1.8BR) are exposed from the center of the D4 magnet to the beam dump with the calculated beam optics and the pencil for comparison. An iron (Fe) target of 2 cm thickness is used for an experimental target located at the final focus point as the most stringent estimate. The results include the safety factor of four, *i.e.*, the calculation results are multiplied by four. The calculated result of the radiation level at the beam height (150-250 cm sliced) is shown as a color map. The east-west dependence of the radiation level at the catwalk position (650-750 cm height) and the up-down dependence at the staircase position are also shown as left and right plots, respectively. At all points outside the experimental area, the radiation level is below the limit of 25 μSv/h.

3.3   Process and Cost

As previously described, the existing CDS for E73 will be replaced by the Hyp-TPC spectrometer for E72 upon completion of E73. After the completion of E72, scheduled for mid FY2025, the K1.8BR modification will begin. The following steps are required to modify the beam line, except for the spectrometer part.

- **D5 Removal** After completing E72 and removing the Hyp-TPC spectrometer, the D5 magnet is removed.

- **Cable Removal** In order to rearrange the shielding in the experimental area, it is necessary to completely remove the cables attached to the shielding. This includes signal cables (BNC and twisted pair), HV cables (SHV), power cables and outlets (AC100V and AC200V), cable racks, and so on. We plan to remove
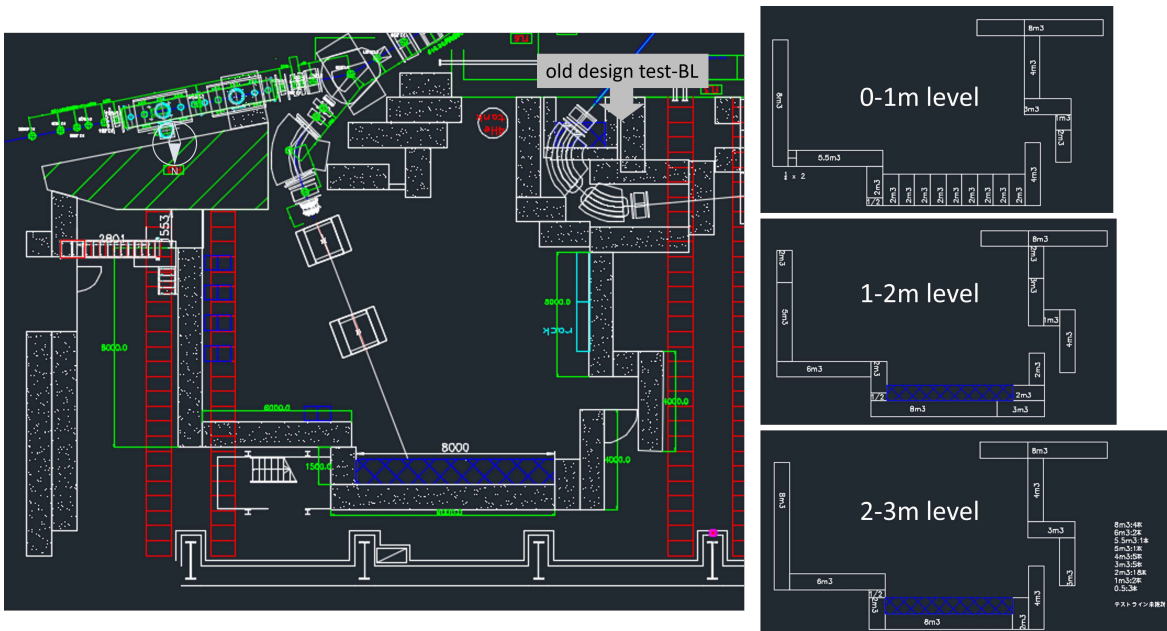
16

Figure 10:   Plan of shield rearrangement using the existing concrete blocks and iron blocks designed by the Hadron Group.

some of the cables by ourselves that are currently unnecessary after E73 ends, but we would like to have a contractor do the remaining work before the shielding is rearranged.

- **Shield Rearrangement** After the cables have been removed, the concrete shields and the iron beam dump are rearranged. Figure 10 shows a plan of the shield rearrangement using the existing concrete blocks and iron blocks designed by the Hadron Group. This makes it possible to rearrange the K1.8BR shields without purchasing new ones.

- **Other Necessary Matters** The PPS and interlock systems are removed during the shield rebuild and must be replaced to accommodate the new shield placement. In addition, optional upgrades to the Q8 magnet are planned in conjunction with the removal of the D5 magnet.

The estimated cost is summarized in Table 4 although it is still a work in progress [‡]. We hope that the cost of the upgrade will be covered by a facility budget.

[‡]Apart from this summary, the optional upgrades to the Q8 magnet will cost approximately 5,000 kJPY.

Table 4: Summary of estimated costs that we hope will be covered by a facility budget.

Item	Cost (kJPY)
D5 removal	1,000
Cable removal [power cable re-installation included]	11,000
Shield rearrangement [maximum estimate]	21,000
PPS and other interlocks rearrangement	5,000
In total [maximum estimate]	38,000

4 Beam Line Spectrometer

A schematic drawing of the beam line spectrometer is shown in Fig. 11. It consists of beam line magnets, trigger counters, a beam line chamber, and a kaon identification counter.

The beam trigger is generated by a coincidence signal from a beam hodoscope tracker (BHT) and a time zero counter (T0); the flight length between the BHT and T0 is 4.0 m. The TOF resolution between the BHT and T0 is expected to be ~ 160 ps (σ), which is sufficient to distinguish between kaons and pions. To select the beam hitting the target at trigger level, a beam definition counter (DEF) is installed just in front of the target at the beam final focus (FF). The kaon beam with momentum around 1.0 GeV/c is identified by rejecting the pion beam using an aerogel Cherenkov counter (AC) with a refractive index of 1.05.
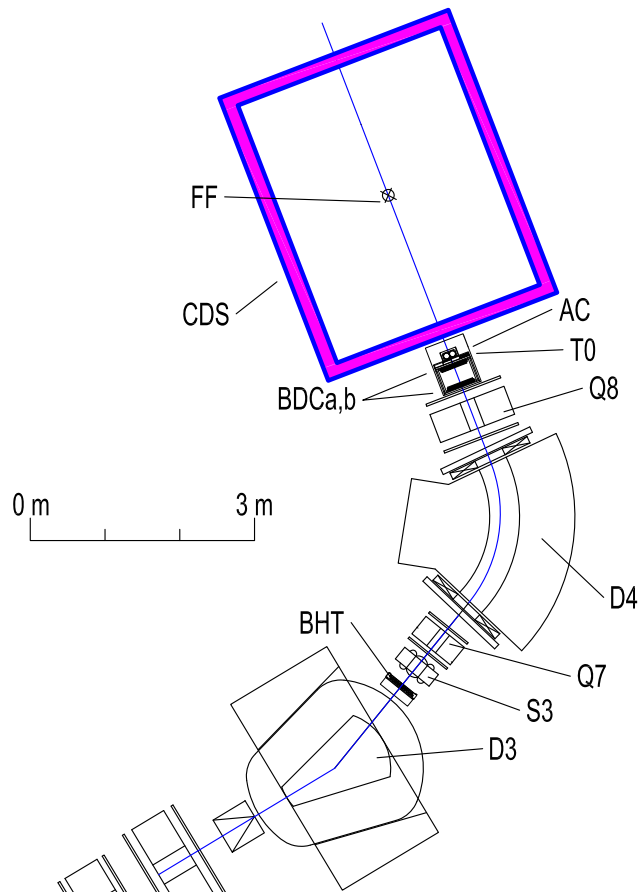

Figure 11: Schematic drawing of the beam line spectrometer consisting of trigger counters (BHT and T0), a beam line chamber (BDC), and a kaon identification counter (AC).
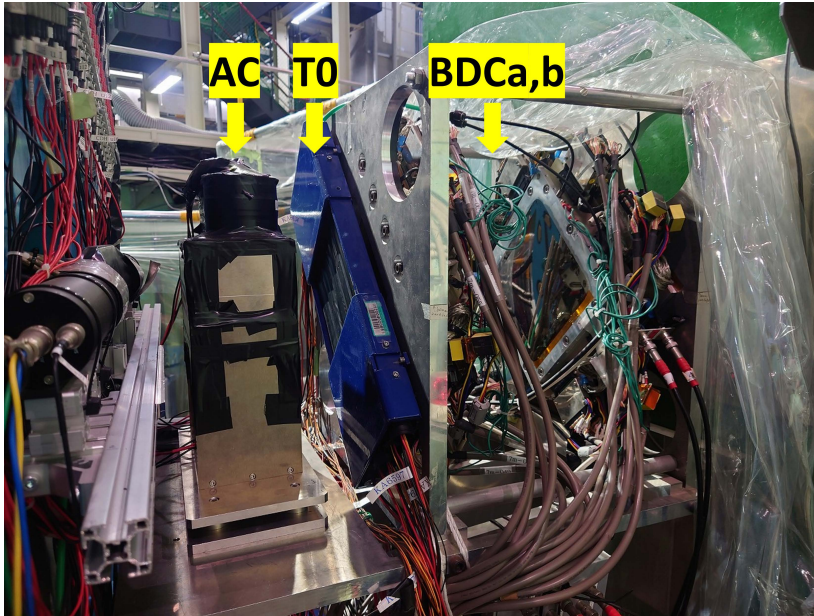
Figure 12: Current setup around the entrance of the existing solenoid magnet, and these detectors will be used as they are in the E80 setup.

The kaon beam is tracked by two beam trackers: the BHT and a beam line chamber (BDC). The momentum of the kaon is analyzed with this tracking information together with the beam optics of the D4 magnet (a second-order transport matrix). The expected momentum resolution is 2×10^{-3}, which is sufficient for E80 as in the case of E15. To determine the reaction vertex, the beam trajectory is also measured by a drift chamber (BPC) just in front of the experimental target.

All of these apparatus are in place and have been well studied on the current K1.8BR beam line. Figure 12 shows the current setup around the entrance of the existing solenoid magnet, and these detectors will be used as they are in the E80 setup.

4.1   Trigger Counters

Beam Hodoscope Tracker (BHT)
The BHT is a segmented plastic scintillation counter located downstream of the D3 magnet. Each scintillator is made of Eljen EJ-228 with a unit size of 150 mm (height) $\times$ 7.5 mm (width) $\times$ 3 mm (thickness). A total of 64 segments are arranged in two staggered layers, each layer having 32 segments with a spacing of 2.5 mm. Therefore, the effective horizontal coverage is 320 mm, and the horizontal position resolution is ~ 0.72 mm ($= 2.5/\sqrt{12}$). The scintillation light is detected by a pair of two 3×3 mm^2 Hamamatsu S13360-3050PE MPPCs (Multi-Pixel Photon Counters) connected in series, mounted at the top and bottom ends, and read with AD8000-based amplifiers.

Time Zero Counter (T0)

T0 is a segmented plastic scintillation counter located downstream of the Q8 magnet. T0 has an effective area of 160 mm (horizontal) × 160 mm (vertical) segmented horizontally into 5 units. The unit size of the Saint-Gobain BC420 scintillator in T0 is 160 mm (height) × 32 mm (width) × 10 mm (thickness). To avoid over-concentration of the beam in one segment, T0 is rotated 45 degrees in the xy plane. The scintillation light is detected by a pair of 3/4 inch Hamamatsu H6612B photomultipliers mounted at the top and bottom ends. Since the coincidence rate of the top and bottom photomultipliers reaches ∼ 1 M counts per spill, the high voltage boosters of all photomultipliers are modified to provide sufficient current to the last three dynodes.

Beam Definition Counter (DEF)

The DEF is installed just upstream of the target vacuum vessel to improve data quality and data acquisition efficiency. In the current and planned magnetic spectrometer setup, less than 50% of the kaon beam hits the liquid target due to the large beam spot size at the final focused point. Therefore, the DEF is used to select the central region of the beam at the trigger level by adding the DEF signal to the beam trigger made by the coincidence signal of the BHT and T0.

A thin scintillation counter array is used for the DEF. The DEF has an effective area of 80 mm (horizontal) × 110 mm (vertical) which is horizontally segmented into 4 units made of Eljen EJ-230 with a unit size of 100 mm (height) × 20 mm (width) × 3 mm (thickness). The scintillation light is detected by a pair of three series-connected Hamamatsu S13360-3050PE MPPCs mounted at the top and bottom ends.

4.2   Kaon Identification Counter

The kaon beam trigger uses an aerogel Cherenkov counter (AC) located downstream of T0. An aerogel radiator with a refractive index of 1.05 is used as a threshold Cherenkov counter to reject pions in the momentum range 0.7 GeV/c to 1.15 GeV/c. The AC has an effective area of 180 mm (width) × 100 mm (height) × 100 mm (thickness), covering the entire distribution of the kaon beam. Cherenkov photons emitted in the beam direction are diffused in the aerogel, reflected by the thin mirror foils surrounding it, and reach four photomultipliers at the top and bottom. Three-inch fine-mesh photomultipliers (Hamamatsu R5543) are used to work with the fringing fields of the Q8 magnet and the CDS magnet. A typical pion detection efficiency is better than 99%. The miss rate of identifying a kaon as a pion is about 1%.

4.3   Beam Line Chambers

Beam Line Chamber (BDC)

The BDC consists of two sets of drift chambers of the same design, BDCa and BDCb, installed ∼ 300 mm apart downstream of the Q8 magnet. The BDC has 8 layers,

$UU'VV'UU'VV'$ configuration, with the wires tilted $\pm$ 45 degrees in the U and V layers. Each layer contains 32 sense wires with a drift length of 2.5 mm, corresponding to an effective area of 160 mm $\times$ 160 mm. The number of readout channels is 256 for both BDCa and BDCb.

The BDC uses 12.5 μm diameter gold-plated tungsten wires with 3% rhenium and 75 μm diameter copper-beryllium wires for the sense and filed wires, respectively. The cathode planes are made of 12.5 μm aluminized Kapton. The readout electronics of both chambers consists of a preamplifier board with amplifier-shaper-discriminator ICs (ASD, SONY-CXA3653Q [42], $\tau = 16$ ns) mounted on the chambers and a TDC. The output signal from the ASD board is sent to the HUL Multi-Hit TDC via 7m long twisted pair cables. The chamber gas is an argon-isobutane mixture passed through a methylal (dimethoxymethane) bubbler at a refrigerator temperature of 4°C with a ratio of 76% (Ar), 20% (isobutane), and 4% (methylal). The operating voltage of the BDC is set at -1.25 kV on both the filed wires and the cathode planes. Typical position resolution of 150 μm and detection efficiency of 99% have been achieved.

Beam Profile Chamber (BPC)

The BPC is installed just upstream of the target cell to precisely determine the reaction vertex point. The BPC is a compact circular planar drift chamber with a diameter of 290 mm and a height of 92.2 mm. The BPC consists of 8 layers ($XX'YY'XX'YY'$) with the wires of the Y layer tilted 90 degrees. Each layer contains 32 sense wires with a drift length of 3.0 mm, corresponding to an effective area of 197 mm in diameter. The number of readout channels is 256. The cathode planes are made of 9 μm carbon-aramid foil, and the sense and filed wires, readout electronics, and gas mixture filled are the same as those of the BDC. The operating voltage of the BPC is set at -1.50 kV on both the filed wires and the cathode planes, with typical position resolution and detection efficiency of 150 μm and 99%, respectively.

5 Cryogenic Target System

The main target nucleus for the E80 experiment is ^{4}He. To achieve a reasonable reaction rate, we use liquid ^{4}He as the target. We use a pulse tube cryocooler system developed for the hypertriton lifetime measurement (J-PARC E73 experiment) and successfully operated at the K1.8BR beam line. The system uses a 4 K pulse tube cryocooler, the Cryomech PT410 cold head with the CPA286i compressor. The system has the capability to liquefy all types of H_2/D_2/^{3}He/^{4}He gas with the same system, so the system is designed to be explosion proof. We will extend the horizontal part of the system to fit the newly constructed CDS. Figure 13 shows a schematic design of the target system with the E80 setup. The system will be installed from downstream of the beam using rails laid on the floor, as is currently the case. The E80 experiment uses a target cell consisting of a Kapton cylinder and CFRP caps developed for the E73, with dimensions of 6.8 cm in diameter and 14.2 cm in length. The achievable temperature of the system is 2.7 K, in which the density of the liquid ^{4}He is 0.144 g/cm^3 with a stability of better than 0.1%.
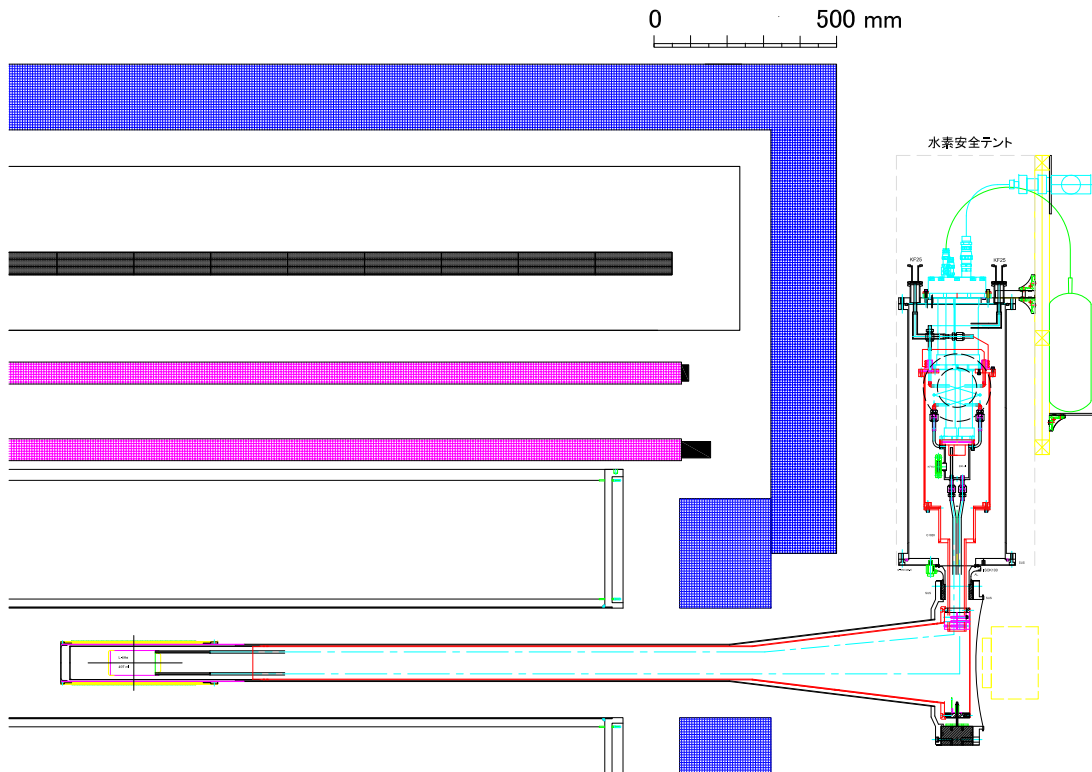

Figure 13: Schematic design of the target system with the E80 setup.

6 Cylindrical Detector System (CDS)

Efficient and high precision reconstruction of decay particles from the target region with large acceptance is a key for the E80 experiment. For this purpose, we are constructing a new large CDS. The requirements for the CDS are as follows:

Large Acceptance

The exclusive measurement of the (K^-, N) reaction is essential for the experiment. To detect as many of the particles involved in the reaction as possible, the detector acceptance must be as large as possible for both charged and neutral particles coming from the target region. The large acceptance system can reduce backgrounds due to misidentification of missing particles.

High Resolution

The spatial and timing resolution of the detector system must be as good as possible to precisely reconstruct the decays of the kaonic nuclei and to determine their properties. At least the resolution achieved with the previously used CDS is required.

Neutron Detection

A high detection efficiency for neutrons is a key in the E80 experiment to precisely measure the $K^-ppn \to \Lambda pn$ decay. The detection of one or more neutrons from production and decay is also of particular importance in the sequence of the experimental programs. In the reconstruction of the decay of $K^-ppn \to \Lambda pn$, the decay neutron has a low momentum of several 100 MeV/c. Therefore, we measure the neutron with the time-of-flight technique using a plastic scintillator, which is the best way to measure the low-momentum neutrons.

To fulfill the requirements described above, the CDS is designed to consist of three main subsystems: a superconducting solenoid magnet, a cylindrical drift chamber (CDC), and a cylindrical neutron counter (CNC). A schematic view of the CDS is shown in Fig. 14. The momenta of the charged particles from the target are reconstructed by the CDC operating in the 0.7 T magnetic field provided by the solenoid magnet. The CNC consists of two separate layers, the first of which is used for charged particle identification and as a decay particle trigger.

For charged particles, the solid angle of the new CDS defined by the first layer of the CNC is 93%, which is significantly larger than the existing CDS of 59%. Figure 15 shows a comparison of the detector acceptance between the new CDS and the existing CDS for the $K^{-4}\text{He} \to \Lambda dn$ channel, evaluated with a full Monte Carlo simulation. The detector acceptance of the new CDS is drastically improved, as can be clearly seen in the figure. The increase in acceptance is essential for the systematic investigation of kaonic nuclei to efficiently detect particles in the final state and to unambiguously specify the reaction channel.

With the goal of efficient neutron detection, the CNC is designed as an array of scintillation counters with a total thickness of 120 mm. The expected neutron detection
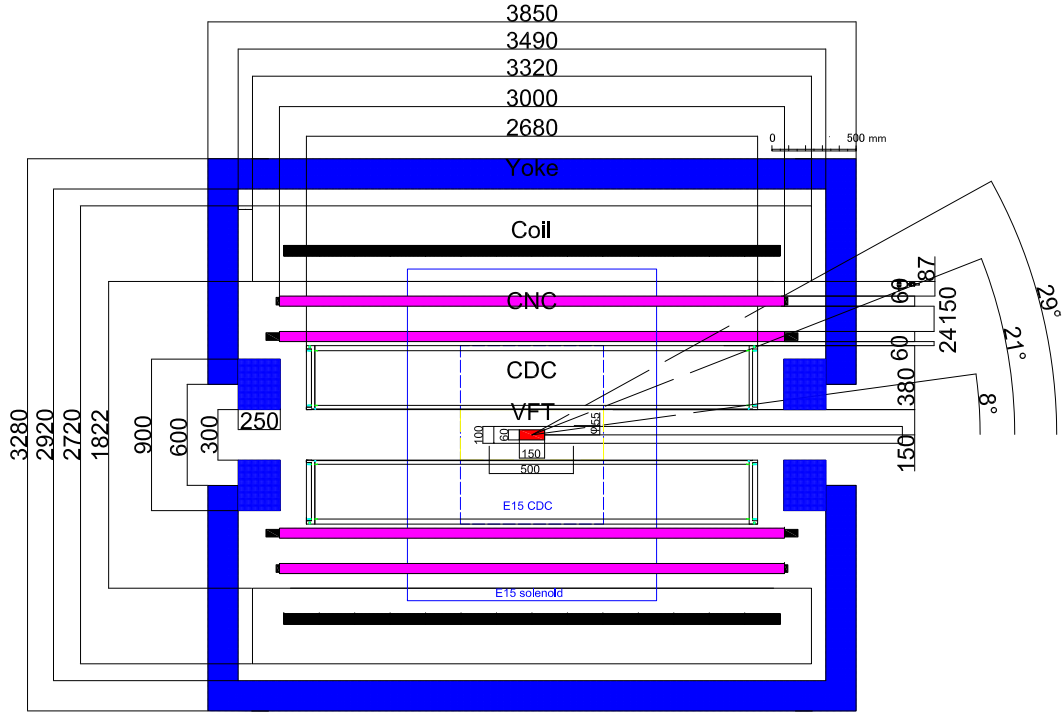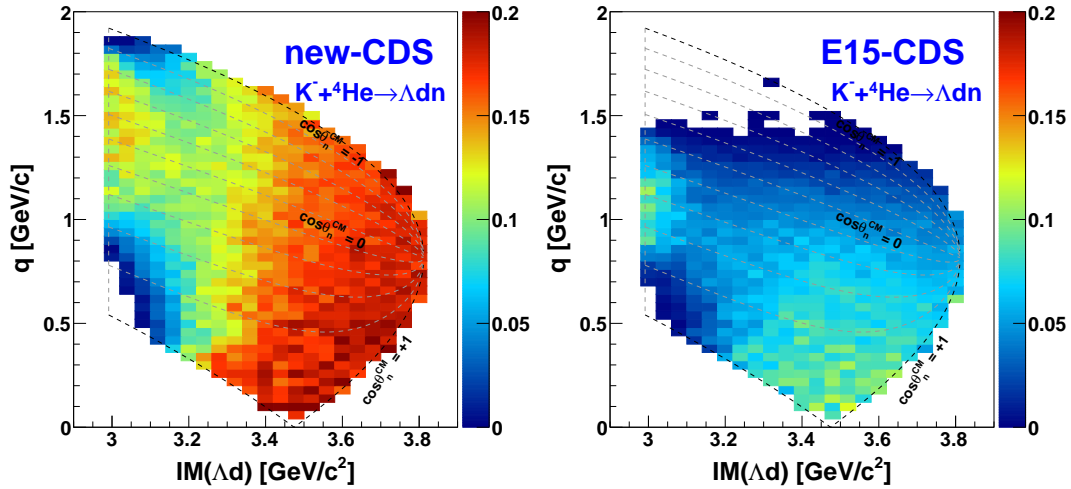
Figure 14: Design of the CDS (cross section).

Figure 15: Detector acceptance for the Λd detection with the CDS in the $K^- + {}^4\text{He} \rightarrow \Lambda dn$ reaction. The left figure shows the acceptance with the newly constructed CDS (new-CDS), and the right figure shows the acceptance with the existing CDS (E15-CDS). The relationship between q and $\cos(\theta_n^{CM})$ is also shown, where $\cos(\theta_n^{CM})$ is the polar angle of the missing neutron in the center of mass frame of the $K^- + {}^4\text{He}$ reactions.

efficiency is $12\% \sim 36\%$ depending on the neutron momentum, four times that of the existing CDS.

The CDS is designed to be easily rearranged to suit individual experimental goals. For the spin/parity determination proposed as the P89 experiment, we plan to install polarimeter trackers between the first and second layers of the CNC and between the second layer of the CNC and the inner wall of the magnet. Using the polarimeter system consisting of the CNC and these trackers, we will measure the spin-spin correlation of a Λ and a proton from the $\bar{K}NN$ decay. The R&D study of the tracker is underway at SMI and INFN-LNF using a straw tube chamber developed for the PANDA experiment at GSI.

6.1   Superconducting Solenoid Magnet

A large superconducting solenoid magnet provides a strong and uniform magnetic field of up to 1.0 T over the tracking volume by covering a large acceptance for outgoing particles from the target region. The magnet is now being manufactured at TOSHIBA with the help of the J-PARC Cryogenics Section. The design of the main components of the "detector solenoid magnet" for the COMET Phase I experiment is adopted for the magnet, taking into account the experimental requirements and the feasibility of construction.

The parameters of the magnet are summarized in Table 5. A component called the cold mass, which combines the mechanical support and cooling structure of coils wound with the NbTi/Cu superconductors, is conduction cooled by the second stage of Gifford-McMahon (GM) refrigerators driven by air-cooled compressors. The thermal radiation shield surrounding the cold mass is also conduction cooled in the first stage of GM refrigerators. The magnet has sufficient cooling capacity for the design heat load (cold mass: 4.2 W, radiation shield: 119 W) by equipping three GM refrigerators. The magnet is operated with a 3 kVA power supply (maximum output: 200A - $\pm$ 15V). The design peak magnetic field on the conductor reaches 1.2 T at an operating current of 189 A, corresponding to the central magnetic field of 1.0 T. The magnet has sufficient margin in superconductivity for load line ratios below 0.3. In the E80 experiment, we will operate the magnet with the central field of 0.7 T to be able to detect low-momentum charged particles, $i.e.$, down to ~ 50 MeV/c in the case of pions. The bore diameter of the vacuum vessel is 1.8 m and the length is 3.3 m with a total weight of 13.9 tons. The shape of the return yoke is square with external dimensions of 3.3 m $\times$ 3.3 m $\times$ 3.9 m and a total weight of 94 tons; the magnets weigh a total of 108 tons.

Table 5: Parameters of the superconducting solenoid magnet.

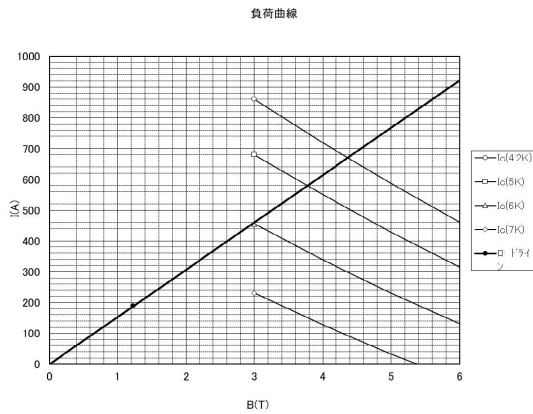|	Items	Unit	Value
Magnet	Center magnetic field	T	1
	Current	A	189
	Coil maximum magnetic field	T	1.23
	Inductance	H	236
	Stored energy	MJ	4.19
	Rise time	h	2
	Cooling method		Small refrigeration machine direct cooling
	Coil protection method		Semi-active quench-back (Self-protection by diode)
Coil	Inner diameter	mm	2,140
	Coil length	mm	170
	Coil thickness	mm	8
	Number of coils	pieces	14
	Total coil length	m	2.92
	Current desity	A/mm^2	131
	Number of turns per coil	turn	944
	Total number of turns	turn	13,216
Superconducting wire	Conductor dimension	mm	1.2
	Copper ratio	Cu/NbTi	4.4
	Length per coil	km	7
	Total length	km	98
Vacuum vessel	Inner diameter	mm	1,808
	Outer diameter	mm	2,720
	Length	mm	3,320
	Barrel thickness	mm	10
	End-plate thickness	mm	50
	Weight (including shield, etc.)	t	10.3
Cold mass	4K weight	t	3.6
Refrigerator	Refrigeration type		Gifford-McMahon (GM) RDE-418D4 (SHI)
	Compressor type		Air-Cooled FA-50 (SHI)
	Number of Refrigerators	unit	3
	Capacity (4.2K)	W	5.4 (=1.8×3)
	Capacity (50K)	W	126 (=42×3)
Heat load	4K section	W	4.2
	Radiation shield section	W	119
Excitation power supply	Power supply type		Kudo Electric Co., Ltd. special order
	Primary input		AC200V, <30A, 50Hz, 3-phase
	Maximum output current	A	200
	Maximum output voltage	V	±15
	Maximum sweeping rate	A/s	0.06
	Cooling method		air cooling
	Quench detector	unit	2 (CLEAR-PLUS 80262)
	Meter relay	unit	2
	Interlock system		abnormal temperature
Return yoke	Inside dimension	mm	2,920
	Outside dimension	mm	3,280
	Length	mm	3,850
	Weight	t	94

Figure 16: Load line of the superconducting wire (T_{cs} = 8.0 K).

Figure 17: Photo of the superconducting coil completed in March 2024.

Superconducting coil

The cold mass consists of a stack of 14 solenoid coils with the same specifications based on 1.2 mm diameter NbTi/Cu wire manufactured by SUPERCON, Inc. Figure 16 shows the load line of the superconducting wire. At the critical value of the wire at 4.2 K, the load ratio is 28% which is sufficiently low. The critical temperature at this operating point (T_{cs}: current sharing temperature) is 8.0 K.

The number of turns for each coil is 944 with a cross sectional configuration of 170 $\times$ 8 mm^2. The length of the superconducting wire for each coil is 7 km. The total number of turns and the length of the wire are then 13,216 and 98 km, respectively. In addition, each solenoid coil is equipped with a 1.5mm diameter copper wire heater for quench protection using a non-inductive winding method. The coil was completed at TOSHIBA in March 2024, as shown in Figure 17.

Quench protection

For quench protection, a semi-active quench-back system is used to reduce the high coil voltage over 1 kV, similar to the MuSIC superconducting solenoid magnet system at the Research Center for Nuclear Physics (RCNP) of Osaka University in Japan [43]. Figure 18 shows the quench protection circuit in which all coils are connected in series with the power supply. Voltage taps are attached to the ends of the solenoid coil and to the splices of the current leads for quench detection and investigation. The series-connected copper quench-back heater path is connected in parallel with the solenoid coil path via diodes. When quench is detected, power is immediately cut off and current in the coils is bypassed to the heater path. Almost all of the energy stored in the magnet is then dissipated into the cold mass.

Figures 19 and 20 show the calculated values of current, coil temperature, quench point temperature, heater temperature, heater voltage, and coil voltage during quench at 1.0 T operation. The current decays from 189 to 0 A in approximately 10 seconds,

including the quench detection time and the quench-back response time. The maximum quench spot temperature is 150 K, the highest temperature in the coils. The maximum heater voltage at both ends of the heater is 450 V, which is equivalent to all coil voltages. These results show that the magnet is safely and reversibly protected.
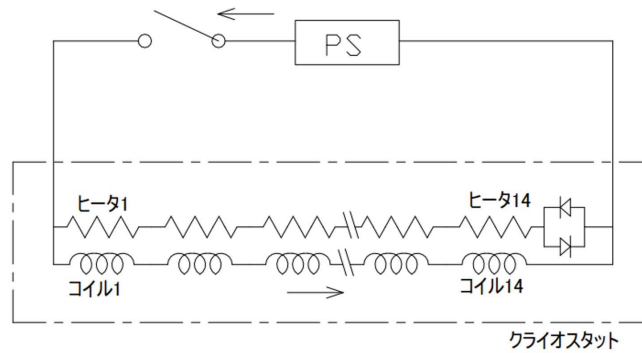

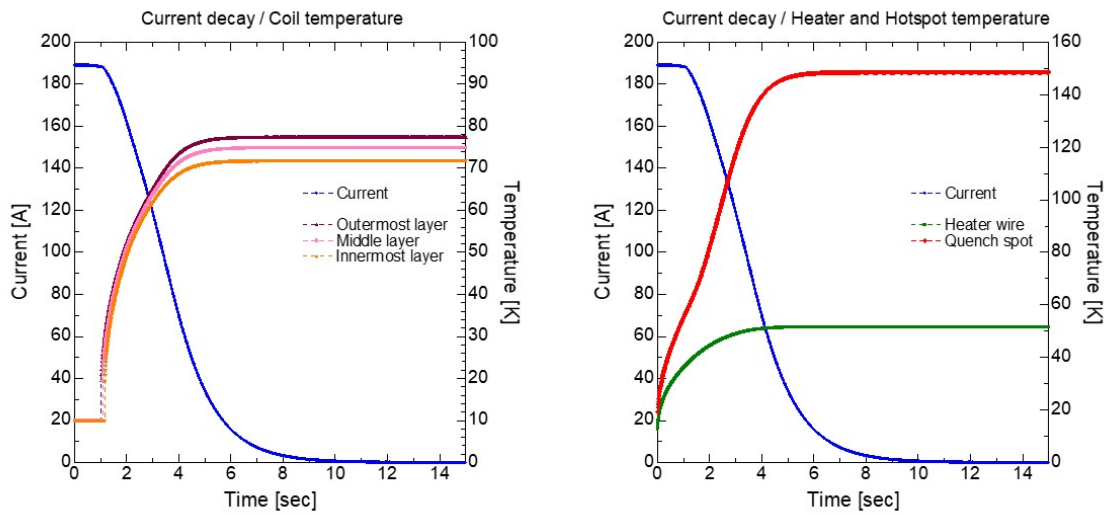Figure 18:   Quench protection circuit.

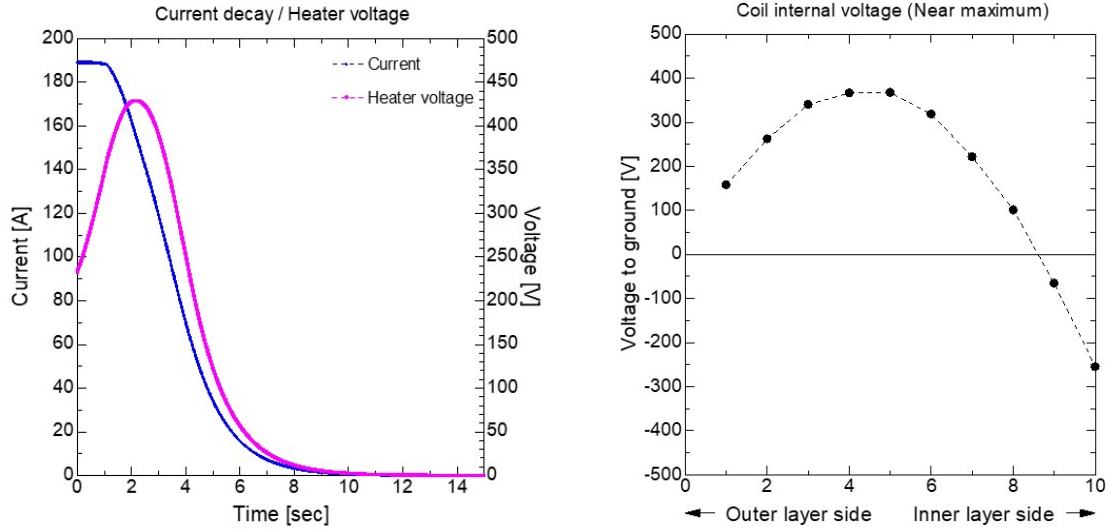Figure 19:   Changes in current, coil temperature, quench point temperature, and heater temperature over time during quench.

Figure 20:   Time variation of current and voltage at both ends of the heater during quench, and coil voltage at quench.

Vacuum vessel

Figure 21 shows a schematic view of the vacuum vessel. To allow the detector to be installed in the magnet bore, base plates are attached to the inner cylinder of the vacuum vessel for a support structure described in Sec. 6.5. The inner cylinder is designed to support a load of 3 tons. As shown in Fig 22, structural calculations using the finite element method show that the maximum displacement of the inner cylinder under load is about 0.3 mm, which is sufficiently small. Construction of the vacuum vessel is scheduled to be completed at TOSHIBA in 2024, followed by magnet assembly and excitation testing without the return yoke at the same factory.

Figure 21: Schematic view of the vacuum vessel. Support structures for the detector system, vessel reinforcements, etc. on the inner wall are not shown.
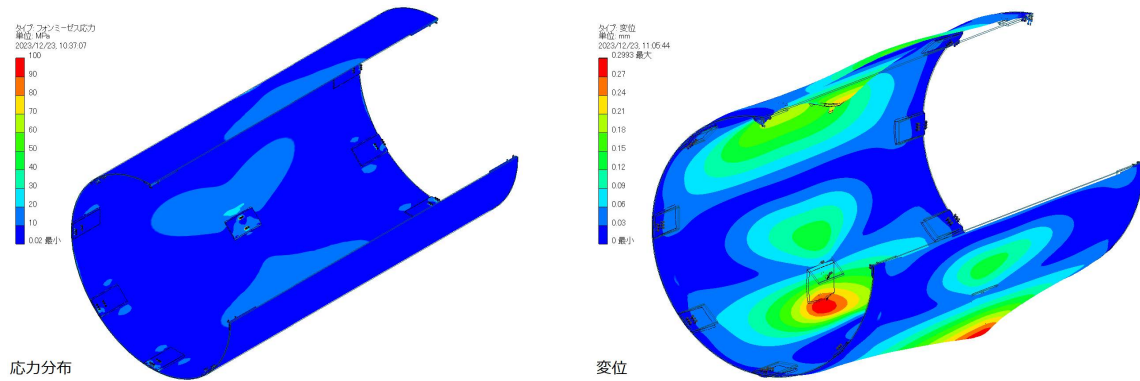
Figure 22: Results of structural calculations of the load on the inner cylinder of the vacuum vessel using the finite element method (Autodesk Inventor 3D-CAD). Stress distribution and displacement are shown. The analysis conditions are as follows: the inner cylinder of the vacuum vessel made of SUS304 is constrained at both end faces, and the detectors (CDC and CNC) with a maximum weight of 2.5 t are loaded through the support structure at a gravitational acceleration of 2 G.

Thermal calculation

Thermal calculations are performed by TOSHIBA based on actual design.

— (1) Heat load —

Table 6 and Table 7 summarize the heat loads to the 4 K section and the radiation shield, respectively. The heat balance using three refrigerators is also shown. The maximum heat load of the 4 K section is estimated to be 4.2 W, including AC losses during ramp-up and ramp-down of current for magnet excitation. The 4 K section heat load during steady operation is 3.5 W, and the cooling capacity with the 2nd stage of the refrigerators has a sufficient margin against the total capacity of 5.4 W. The cooling capacity with the 1st stage of the refrigerators of 126 W also sufficiently exceeds the heat load on the thermal shield of 119 W. Figure 23 shows the temperature map of the refrigerators with the expected operating point. The temperatures of the first and second cooling stages are expected to be about 45 K and 4.2 K, respectively.

Table 6:   Heat load calculation results for the 4 K section.

4 K section heat load (Unit:W)			
Item	Route	Heat load	Remarks
Thermal shield	Heat radiation	2.44	0.05 W/m^2
Supports	Heat transfer	0.75	
Current leads	Heat transfer + Ohmic heating	0.13	HTS lead
Residual gas	Heat transfer	0.10	
Pre-cooling tube etc.	Heat transfer	0.05	ϕ12
Measurement lines	Heat transfer	0.05	
Coil	AC loss	0.70	2h rise time
Radiation	Heat generation	-	
In total		4.2	

Refrigeration capacity (4 K)			
Model	RDE-418D4	1.8	W @ 4.2 K
Number of units		3	
total capacity		5.4	

Table 7: Heat load calculation results for the radiation shield.

Radiation shield heat load (Unit:W)			
Item	Route	Heat load	Remarks
Thermal shield	Heat radiation	84.4	1.5 W/m^2
Supports	Heat transfer	5.1	
Current leads	Heat transfer + Ohmic heating	24.8	Cupper lead
Residual gas	Heat transfer	1.9	
Pre-cooling tube etc.	Heat transfer	2.4	$\phi 12$
Measurement lines	Heat transfer	0.3	
Coil	AC loss	-	
Radiation	Heat generation	-	
In total		119	

Refrigeration capacity (50 K)			
Model	RDE-418D4	42	W @ 50 K
Number of units		3	
total capacity		126	
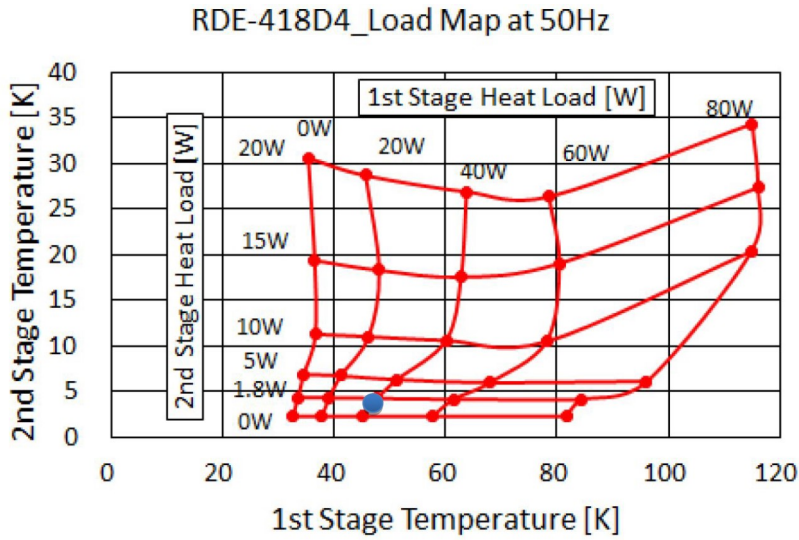
Figure 23: Temperature map of the refrigerators. The expected operating point of the refrigerator is shown as a blue filled circle.
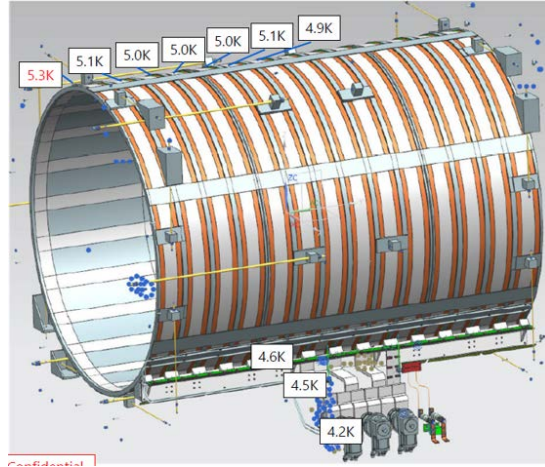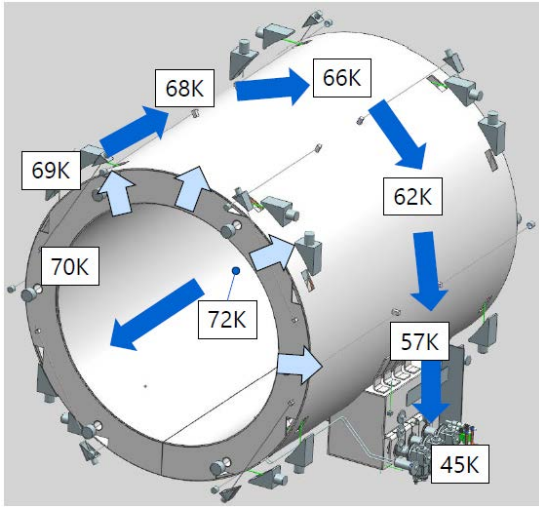
Figure 24: Radiant shield heat transfer path and temperature distribution.

Figure 25: 4 K section heat transfer path and temperature distribution.

— (2) Temperature distribution at the radiation shield —

The aluminum alloy heat shield structure is designed to be cooled entirely by material heat conduction from the cold head of the refrigerators. The thermal shield temperature gradient is estimated based on the thermal resistance of the heat conduction path. The heat transfer path is calculated from the refrigerators to the farthest point of the center of the inner cylinder in the order shown in Fig. 24.

1. inner cylinder center (72 K) $\rightarrow$ end plate on inner cylinder side (70 K)
2. end plate on the inner cylinder side (70 K) $\rightarrow$ end plate on the outer cylinder side (69 K)
3. outer cylinder at each 45° point by inserting heat transfer from the end plate:
   - 0° (69 K) – 45° (68 K)
   - 45° (68 K) – 90° (66 K)
   - 90° (66 K) – 135° (62 K)
   - 135° (62 K) – 180° (57 K)
4. shield flexible welded part (57 K) $\rightarrow$ 1st-stage $\rightarrow$ refrigerator flexible part $\rightarrow$ refrigerator (45 K)

There is a temperature difference of 27 K (= 72 K - 45 K) from the refrigerators to the farthest point of the center of the inner cylinder, which is within the acceptable range.

— (3) Temperature distribution at the 4 K section —

Each coil conduction cooling structure consists of cooling strips made of high purity aluminum with a thermal conductivity of approximately 4,000 W/m·K. The temperature difference from the refrigerator to the farthest coil surface is calculated from the thermal resistance as shown in Fig. 25.
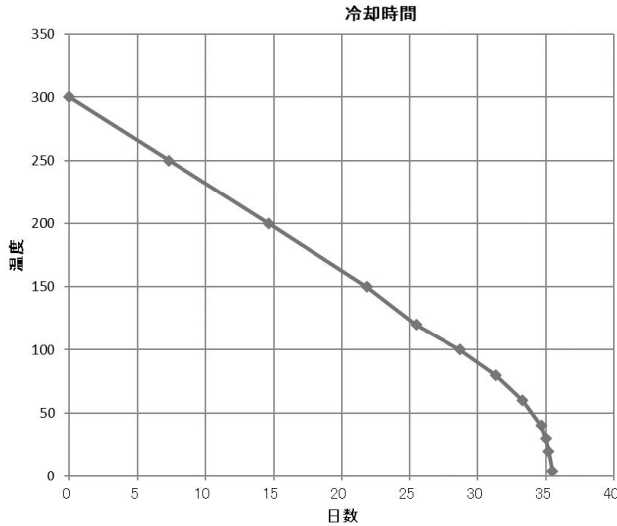
Figure 26: Estimated cooling time.

Figure 27: Power supply for the superconducting solenoid magnet.

1. farthest coil surface (5.3 K) → 4 K cooling plate (4.6 K)
2. 4K cooling plate (4.6 K) → 4K flexible part (4.5 K)
3. 4K flexible part (4.5 K) → refrigerator cold head (4.2 K)

There is a temperature difference of 1.1 K (= 5.3 K - 4.2 K) from the coil surface to the refrigerator. This provides a sufficient temperature margin; the maximum temperature of the 4 K section is 5.3 K, while the critical coil temperature is 8.0 K.

— (4) Cooling time —

Figure 26 shows the estimated cooling time using only the refrigerators. The estimated cooling time from room temperature to 4 K using only the refrigerators is approximately 36 days. The initial cooling time from room temperature to 100 K using liquid nitrogen in pre-cooling tubes is expected to be approximately 7 days based on the results of other superconducting magnets, and the cooling time from 100 K to 4 K is approximately 7 days from Fig. 26. Therefore, the cooling time using liquid nitrogen and the refrigerators is estimated to be approximately 14 (= 7 + 7) days. Note that in the pre-cooling method using the pre-cooling tubes, there is no temperature difference that could damage the equipment regardless of the cooling rate, so there is no limit to the allowable temperature difference between each part.

Power supply and DAQ

We use a dedicated power supply for the superconducting solenoid magnet manufactured by Kudou Electric Co., Ltd. The power supply provides stable DC current up to 200 A / ± 15 V within a current ripple of 1×10^{-4} peak-to-peak. The maximum sweep rate is 0.06 A/s, where we will use a setting of 0.03 A/s, so the excitation time

is ~ 2 hours.

To monitor the coil voltage, we use an OMNIACE RA3100 system as a fast DAQ system, capable of capturing fast switching waveforms and fast transient events. When a quench occurs, a signal from the quench detector (CLEAR-PULSE 80262) shuts down the power supply and disconnects power from the magnet. These sequential events are recorded by the fast DAQ system. Coil temperature is also monitored using a slow DAQ system to read 14 CERNOX cryogenic temperature sensors mounted on each coil and thermocouple thermometers.

The power supply (Fig. 27) and the DAQ systems are already in place.

Return yoke

The return yoke consists of a square side wall and end caps as shown in Fig. 28. Each side of the side wall is divided into three parts, for a total of 12 pieces, so that it can be easily hoisted by a 40 ton overhead crane at the Hadron Hall. The end cap is divided into two pieces, top and bottom, and is opened and closed by the crane. To make the magnetic field uniform in the tracking region, ring-shaped yokes are installed inside the two end caps. A refrigerator port is provided in the center of the side wall for installation of the GM refrigerators. The vacuum vessel, ports, cold head, etc. are designed so that they do not protrude beyond the return yoke. The detector readout cables exit through holes in the four corners of the end caps. The return yoke was manufactured by System & Project Engineering Co., Ltd. and completed in March 2023 as shown in Fig. 29. It is now stored at the KEK Tuskuba Campus after being disassembled.

SS400 plates are used for return yoke irons. Table 8 summarizes the inspection certificates of the SS400 plates used for the return yoke. The basic performance of SS400 was examined by the COMET group using SS400 samples from various companies for the COMET experiment. We use SS400 plates from "Nippon Steel" and "Kobe Steel", which are the same types of SS400 plates used by the COMET group. The results of B-H curve measurements on SS400 from "Nippon Steel" and "Kobe Steel" are shown in Fig. 30, with the permission of the COMET group. There is no significant difference in the use of different SS400 at the level we are concerned with.
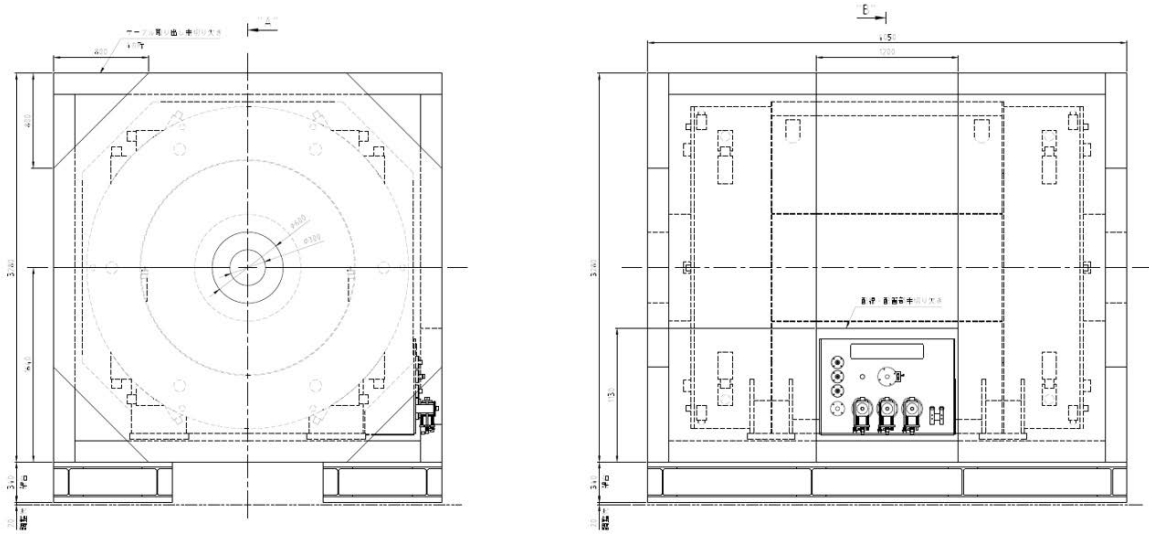
Figure 28:   Schematic view of the return yoke.

Figure 29:   Photo of the completed return yoke at a manufacturing factory.

Table 8: Inspection certificates for the SS400 plates used for the return yoke.

| Inspection Certificate No.	Quantity	Plate No.	Manufacturer	Part Name	Yield Point, Yield Stress (N/mm2)	Tensile Strength	Elongation (%)	C	Si (x1/100)	Mn	P	S (x1/1000)
P-01	1	809070661	Nippon Steel	bottom-1, bottom-3	253	428	36	15	18	94	11	4
P-02	1	809060301	Nippon Steel	bottom-2, side-6	253	428	33	15	18	94	11	4
P-03	1	809101341	Nippon Steel	side-1, side-3	238	427	37	16	17	95	9	3
	1	809101361			238	427	37	16	17	95	9	3
P-04	1	862302501	Nippon Steel	side-2, top-2	238	427	37	16	17	95	9	3
	1	809070641			253	428	36	15	18	94	11	4
P-05	1	809101341	Nippon Steel	side-4, side-5, top-1, top-2	238	427	37	16	17	95	9	3
	1	809101361			238	427	37	16	17	95	9	3
P-06	1	809070701	Nippon Steel	upstream-yokes, downstream-yokes	253	428	33	15	18	94	11	4
	1	809070801			253	428	33	15	18	94	11	4
P-07	2	437851001-02	Nippon Steel	base frame	292	460	36	17	21	88	18	4
P-08	2	640110409-10	Nippon Steel	base frame	274	428	34	18	16	49	17	4
	1	640110412			273	429	31	18	16	49	17	4
	5	640110412-16			254	421	32	18	17	48	16	5
P-09	4	838350401-04	Nippon Steel	base frame	259	426	34	18	16	46	17	6
P-10	6	437850303-08	Nippon Steel	base frame	267	431	33	18	10	50	20	5
	1	437850502			263	429	36	18	17	47	17	6
P-11	5	640110108-12	Nippon Steel	base frame	311	453	31	18	9	49	18	5
	2	640110215-16			287	428	31	17	9	48	21	6
P-12	1	1989841	Kobe Steel	donut yokes	235	445	30	21	13	75	17	8
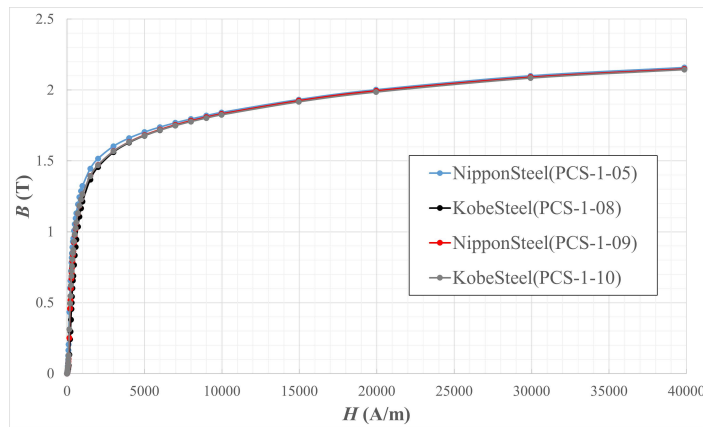
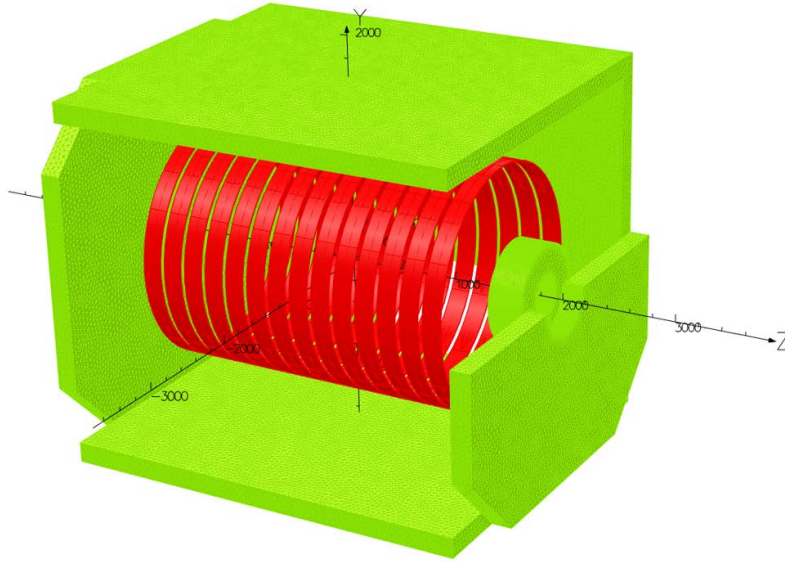Figure 30: B-H curve of SS400 from "Nippon Steel" and "Kobe Steel" studied by the COMET group.

Figure 31: Magnetic field calculation model. Part of the return yoke is shown. The beam direction defines the z-axis direction in right-handed coordinates with the y-axis pointing up.

Magnetic field calculation

The magnetic field distribution is calculated with a full-scale 3D magnet model using the OPERA simulation software package as shown in Fig. 31, where the beam direction defines the z-axis direction in right-handed coordinates with the y-axis pointing up. The maximum field is set to 1.0 T for all magnetic field calculations. The magnetic field distribution for the z-component (beam direction), B_z, is shown in Fig. 32. In the tracking region ($r \lesssim 500$ mm), the magnetic field uniformity is a few percent near the central region ($|z| \lesssim 800$ mm), but decreases at the edges ($800 \lesssim |z| \lesssim 1300$ mm) where a simple helix fit is not applicable. Figure 33 shows the magnetic field distribution around the GM refrigerator cold head motors ($x \sim 1518$ mm, $y \sim -1190$ mm). The magnetic field at the center of the motors is less than 20 mT, which is below the operating limit of 50 mT.

Charged particle tracking will be performed using the Runge-Kutta method or the Kalman filter based on the calculated magnetic fields. To verify the magnetic field calculation, we plan to measure the magnetic field with a 3D Hall probe after the magnet system is completed at J-PARC, as described later.
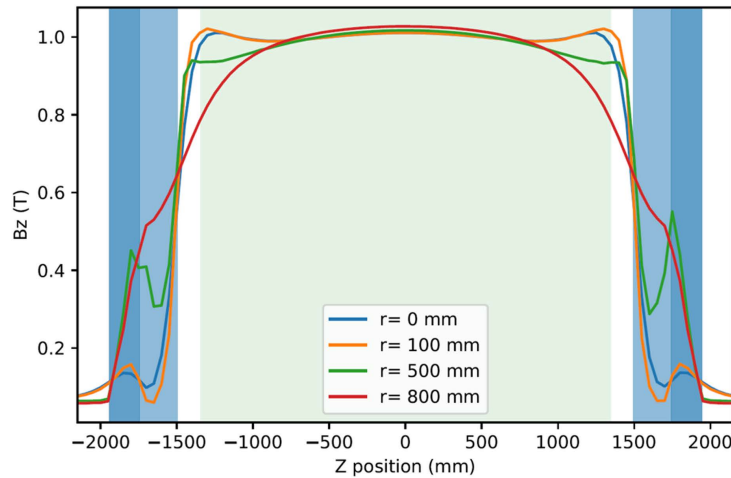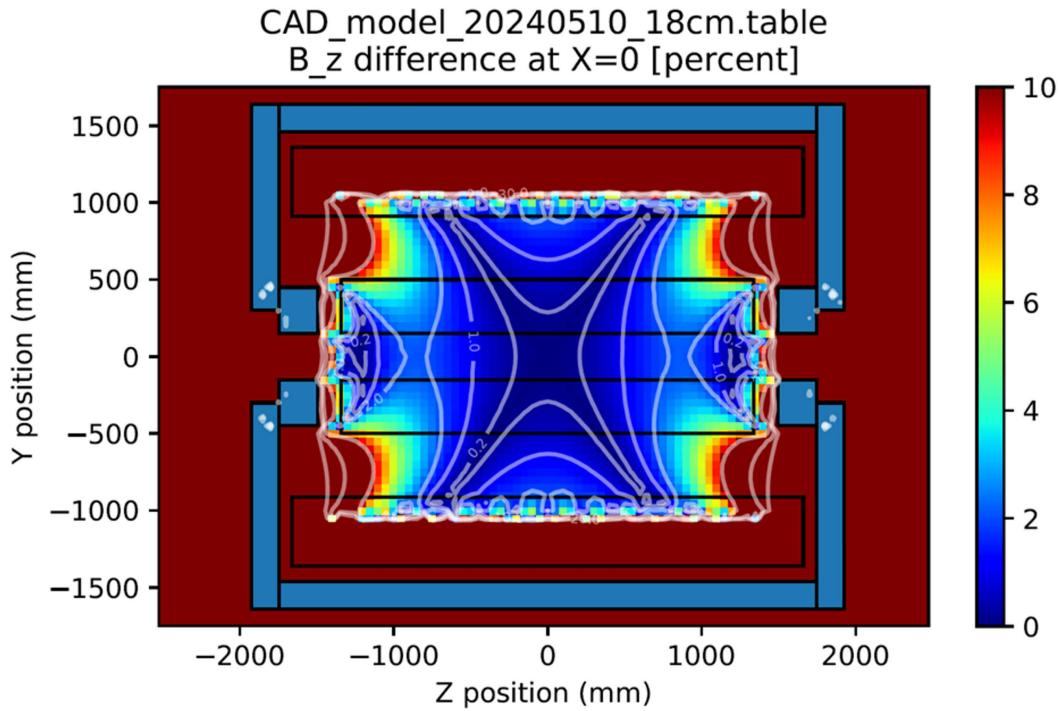
Figure 32: Calculated magnetic field distribution. (left) The z-component of the magnetic field, B_z, in the (z, y) plane on the central beam axis. The deviation from the central magnetic field is shown as a percentage. (right) The position dependence of B_z as a function of the z-axis: $r = 100, 500, 800$ mm correspond to the position 50 mm inside the inner wall of the CDC, 30 mm inside the outer wall of the CDC, 100 mm inside the vacuum vessel.
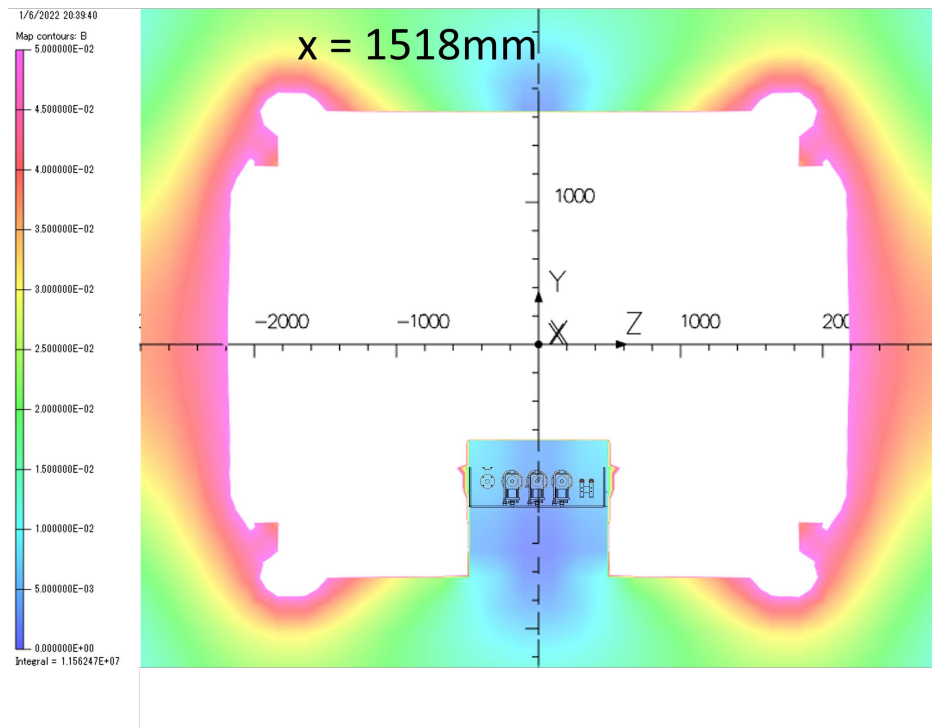
Figure 33: Calculated magnetic field distribution around the GM refrigerator cold head motors ($x \sim 1518$ mm, $y \sim -1190$ mm). In the (z, y) plane cross section at $x = 1518$ mm, below 50 mT is shown in the color map. The magnetic field at the center of the motors is less than 20 mT, which is below the operating limit of 50 mT.

Structural analysis

Structural calculations of the forces on the magnet yoke are performed to confirm safety. The results of the structural analysis are described below in the following order. (1) The electromagnetic force applied to the return yoke is first evaluated using OPERA. (2) Using the calculated electromagnetic force, the effects on the end caps of the return yoke are evaluated by the finite element method using Autodesk Inventor 3D CAD, and the effects on the entire return yoke are also estimated by hand. (3) Finally, the seismic analysis is performed by hand calculation.

— (1) Electromagnetic force —

Figure 34 summarizes calculated electromagnetic force applied to each piece of the return yoke using the OPERA simulation software package. For the side yokes, the electromagnetic force that pulls them inward is about 40 tons maximum per side. For the upstream and downstream end caps, the force that pulls the end caps inward is about 100 tons.

Figure 34: Summary of the calculated electromagnetic force applied to each part of the return yoke using the OPERA simulation software package.
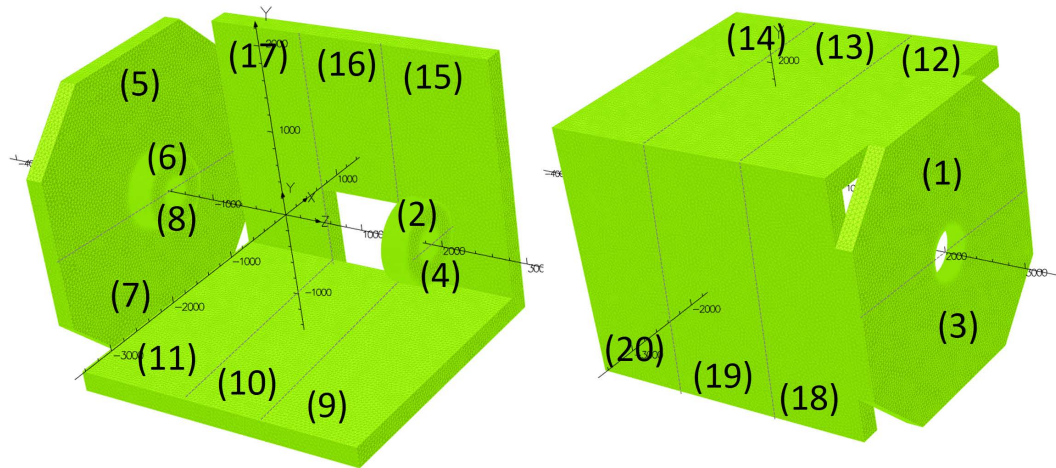
component name	Fx [N]	Fy [N]	Fz [N]
(1) cap down bottom	2	25,452	-759,143
(2) donut down bottom	107	19	206,973
(3) cap down up	29	-25,644	-776,760
(4) donut down up	107	19	206,973
(5) cap up bottom	22	25,536	757,753
(6) donut up bottom	131	-356	-206,821
(7) cap up up	116	-25,293	777,720
(8) donut up up	131	-356	-206,821

component name	Fx [N]	Fy [N]	Fz [N]
all coils (Lorentz force)	-390	226	-103

component name	Fx [N]	Fy [N]	Fz [N]
(9) bottom down	-36	22,811	-153,692
(10) bottom middle	160	622	-250
(11) bottom up	-28	22,564	153,750
(12) top down	6	-13,595	-110,830
(13) top middle	17	-876	-17
(14) top up	4	-13,672	110,961

component name	Fx [N]	Fy [N]	Fz [N]
(15) left down	-7,508	-9,926	-64,584
(16) left middle	-525	39	-166
(17) left up	-7,512	-9,660	63,407
(18) right down	7,603	692	-79,596
(19) right middle	619	22	13
(20) right up	7,602	730	79,782

Table 9: Summary of allowable stress limits for SS400 and SCM435 [44].

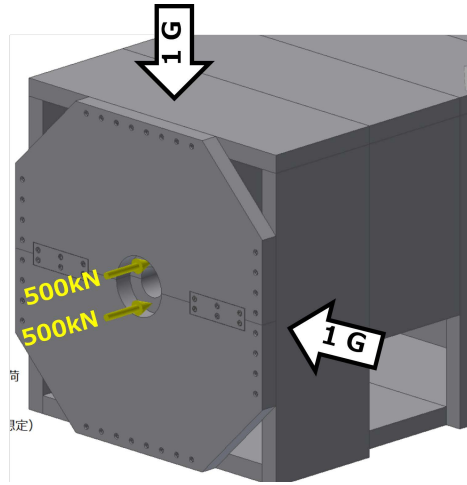|	Yield point		Allowable stress for temporary (seismic) loading			Allowable stress for sustained loading		
	SS400	**SCM435**		**SS400**	**SCM435**		**SS400**	**SCM435**
	F (N/mm2)	F (N/mm2)		(N/mm2)	(N/mm2)		(N/mm2)	(N/mm2)
Compressive/tensile stress (圧縮/引張応力)	245	930	F	245	930	F/1.5	163	620
Bending stress (曲げ応力)	245	930	F	245	930	F/1.5	163	620
Shear stress (せん断応力)	245	930	F/√3	141	537	F/(1.5*√3)	94	358

Figure 35: Analysis conditions for securing the end caps to the side yokes using the Autodesk Inventor 3D CAD application. The analysis is performed by applying a force of 500 kN to the upper and lower end caps at a single point near the center as shown. Gravity of 1.0 G is also applied from the vertical and horizontal directions. The constraint condition is the bottom of the return yoke.

— (2) Effects of electromagnetic force on the return yoke —

Based on the electromagnetic force calculations, the stresses and displacements for the end caps are calculated by the finite element method using the Autodesk Inventor 3D CAD application. The calculation uses SS400 as the material whose allowable stress limit is shown in Table 9 together with that of SCM435. The analysis is performed by applying a force of 500 kN to the upper and lower end caps at a single point near the center as shown in Fig. 35, which is an extreme assumption for safety. Gravity of 1.0 G is also applied from the vertical and horizontal directions, the latter assuming an earthquake. The constraint condition is the bottom of the return yoke.

Figure 36 shows the calculated results. The end caps and side yokes are secured with 44 M36 bolts, and the end caps are secured together with 12 M36 bolts. In this configuration, the maximum (tensile) stress on a bolt is 224 MPa, which can be met by using SCM435 M36 bolts with a safety factor of 2.8 (= 620 / 224). The thread shear stress is estimated to be 70 N/mm^2, which gives a safety factor of 5.1 (= 358 / 70), with the following parameters:

- Tensile stress: T = 224 N/mm^2
- Bolt size: M36
- Nominal diameter: ND = 36 mm
- Cross section to ND: A_{ND} = 1018 mm^2
- Effective thread length: L = 29 mm
- Material: SCM435
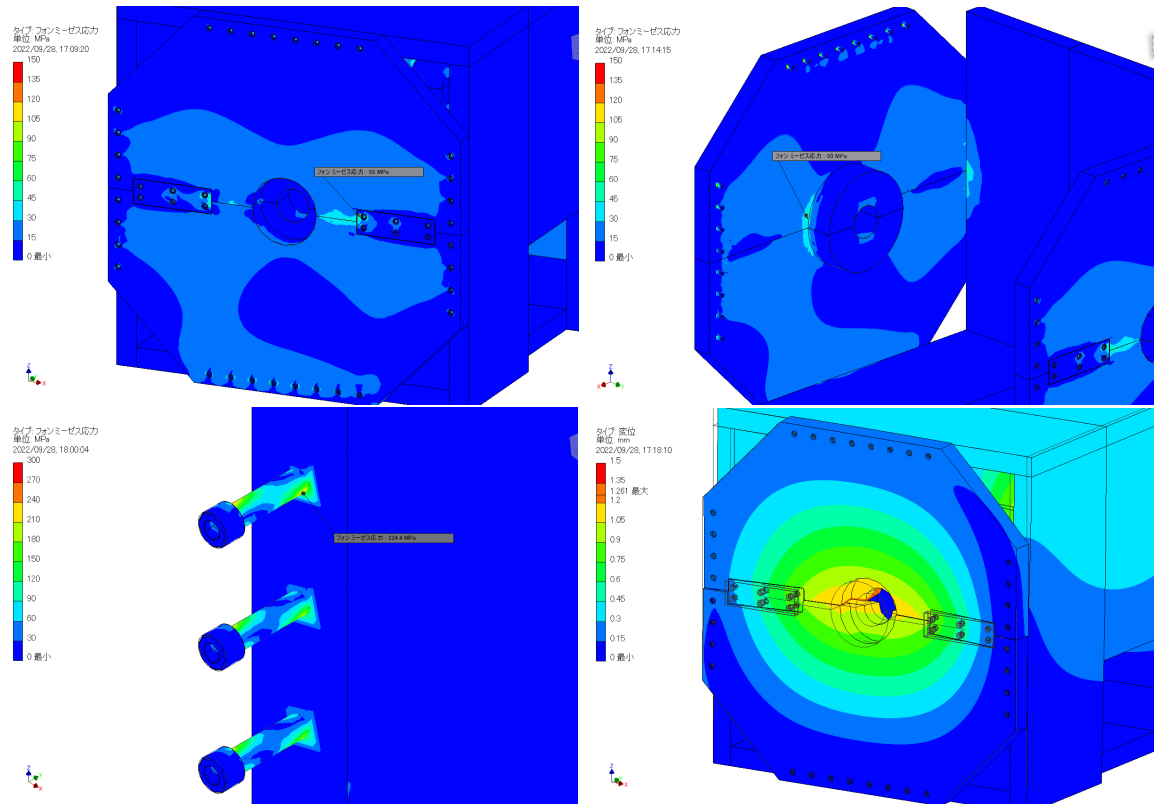- □ Load per bolt: F = T × A_{ND} = 228,004 N

Figure 36:   Calculated stresses and displacements for the end-cap using Autodesk Inventor 3D-CAD application.

☐ Area under load: $A = \pi \times ND \times L = 3279.8$ mm^2

☐ Thread shear stress: $F / A = 70$ N/mm^2

The displacement is 1.26 mm near the center, which is small enough to not cause a problem for the detector inside.

The effect of the magnetic force on the entire return yoke is also estimated by hand, assuming worst case conditions: a maximum force of 40 tons in the x/y direction and 100 tons in the z direction with both ends fixed and a concentrated load in the center. The condition is summarized in Fig. 37. Based on this condition, the bending stress is estimated using the following equations:

- Moment: $M = 1/8 \times L \times F$
- Section modulus: $Z = 1/6 \times W \times T^2$
- Bending stress: $S = M / Z$

Table 10 summarizes the results, where sufficient safety factors are ensured. Thus, the design is strong enough to withstand the load of the electromagnetic force.

Material = **SS400**	Width [W] (mm)	Thickness [T] (mm)	Length [L] (m)	Magnetic force [F] (kN)
Top	1090	180	3100	392
Right	1075	180	3150	392
Left	1075	180	3150	392
Upstream	840	180	3100	981
Downstream	840	180	3100	981
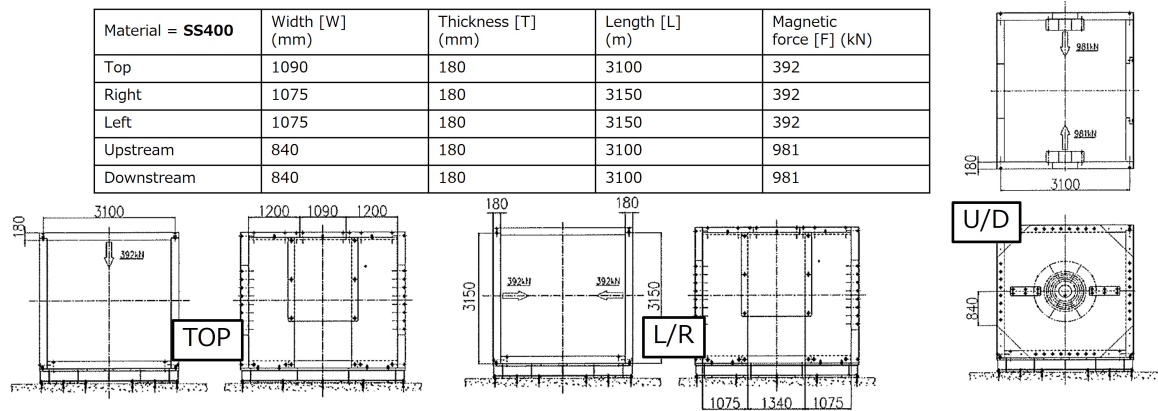
Figure 37: Analysis condition of the effect of the magnetic force on the entire return yoke, assuming the worst case: a maximum force of 40 tons in the x/y direction and 100 tons in the z direction with both ends fixed and a concentrated load in the center.

Table 10: Estimated result of the effect of the magnetic force on the entire return yoke.

Material = **SS400**	Moment [M] (N mm)	Section modulus [Z] (mm3)	Bending stress [S] (N/mm2)	**Safety factor**
Top	151,900,000	5,886,000	25.8	**6.3**
Right	154,350,000	5,805,000	26.6	**6.1**
Left	154,350,000	5,805,000	26.6	**6.1**
Upstream	380,137,500	4,536,000	83.8	**1.9**
Downstream	380,137,500	4,536,000	83.8	**1.9**

— (3) Seismic analysis —

The seismic analysis is performed by hand calculation. The horizontal acceleration of 0.4 G ($\sim$ 400 gal) is assumed as the seismic force with own load; the weight of the return yoke and the solenoid magnet of 115 tons and 20 tons, respectively, are used in the calculation.

(3-a) Earthquake resistance to overturning

First, we estimate the possibility of the return yoke overturning during an earthquake by applying the horizontal acceleration of 0.4 G to the side yoke as shown in Fig 38. The analysis conditions and results are as follows:

- Weight (yoke+solenoid): W = 135,000 kgf
- Vertical distance from floor to center of gravity: L_V = 1898.7 mm
- Horizontal distance from edge to center of gravity: L_H = 1640 mm
- Horizontal acceleration: F = 0.4 G
- □ Overturning moment: M_o = W $\times$ L_V $\times$ F = 102,528 kgf m
- □ Moment of resistance: M_r = W $\times$ L_H = 221,400 kgf m

The result is $M_o < M_r$ with a safety factor of 2, so the return yoke will not fall over in a 0.4 G earthquake.

(3-b) Earthquake resistance of anchor bolts

The stress on anchor bolts shown in Fig 39 is estimated with the following parameters:

- Weight (yoke+solenoid): W = 135,000 kgf
- Bolt size: M24
- Effective diameter: 22.051 mm
- Cross section: A = 381.9 mm^2
- Number of bolts: N = 24
- Material: SS400
- Horizontal acceleration: F = 0.4 G
- □ Shear stress: W $\times$ F / (A $\times$ N) = 57.8 N/mm^2

Therefore, the bolts will not shear with a safety factor of 2.4 (= 141 / 57.8).

(3-c) Earthquake resistance to overturning during assembly

We also estimate the seismic resistance when assembled without end caps. Here 1 section of the return yoke with a width of 1200mm is used as shown in Fig 40. The analysis conditions and results are as follows:

- Weight (top+L+R): W = 15,131.1 kgf
- Vertical distance from floor to center of gravity: L_V = 1917.2 mm
- Horizontal distance from edge to center of gravity: L_H = 1640 mm
- Horizontal acceleration: F = 0.4 G
- □ Overturning moment: M_o = W $\times$ L_V $\times$ F = 11,604 kgf m
- □ Moment of resistance: M_r = W $\times$ L_H = 24,815 kgf m

The result is $M_o < M_r$ with a safety factor of 2, so the return yoke will not fall over
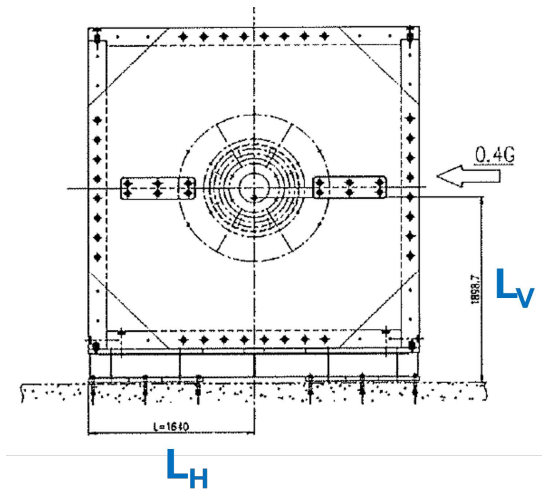
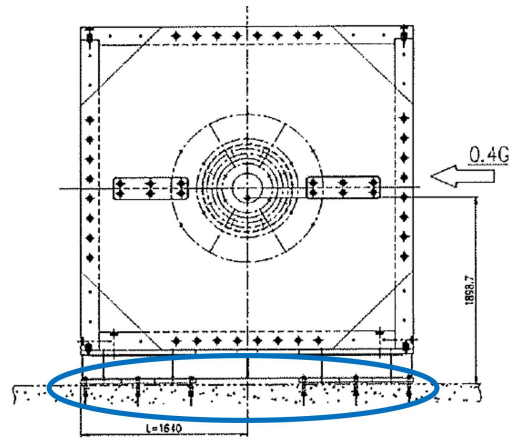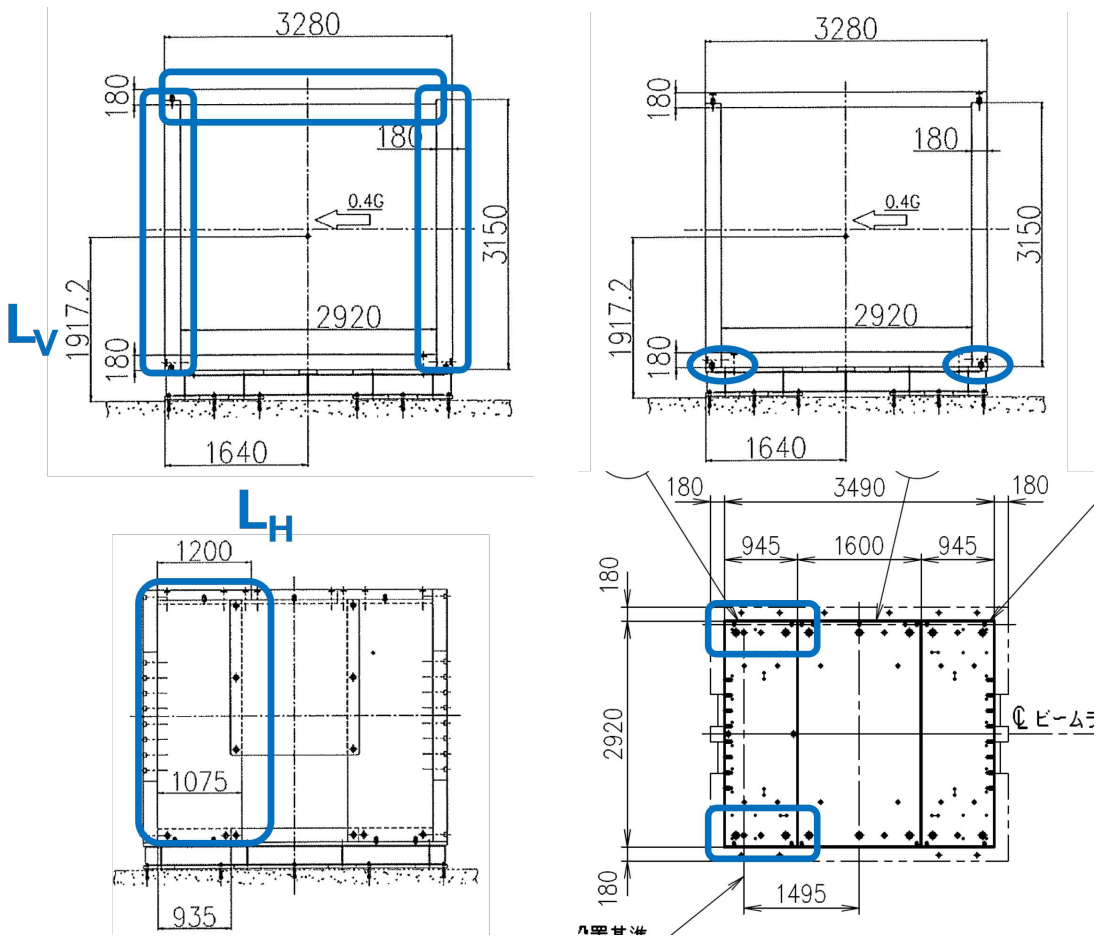Figure 38: Analysis conditions for earthquake resistance to overturning.

Figure 39: Analysis conditions for earthquake resistance of anchor bolts.

during assembly.

(3-d) Earthquake resistance of securing bolts during assembly

The stress on the securing bolts at the bottom yokes is estimated without end caps, with 1 section of the return yoke of 1200mm width shown in Fig 41. The analysis conditions and results are as follows:

- Weight (top+L+R+bottom): W = 18,988.9 kgf
- Bolt size: M30
- Effective diameter: 27.727 mm
- Cross section: A = 603.8 mm^2
- Number of bolts: N = 4
- Material: SS400
- Horizontal acceleration: F = 0.4 G
- □ Shear stress: W × F / (A × N) = 30.8 N/mm^2

Therefore, the bolts will not shear with a safety factor of 4.6 (= 141 / 30.8).

(3-e) Strength of the base frame

Finally, the compressive stress is evaluated for the base frame components shown in Fig. 42. Structural H steels (H250 x 250 x 9 x 14, SS400) are used, but the rib material is not considered to be on the safe side. The parameters used for the calculation are summarized in Table 11. The compressive stress of M / S = 9.9 N/mm^2 is obtained, which gives a safety factor of 16.5 (= 163 / 9.9).

Thus, the return yoke is strong enough to withstand an earthquake.

Figure 40: Analysis conditions for earthquake resistance to overturning during assembly.

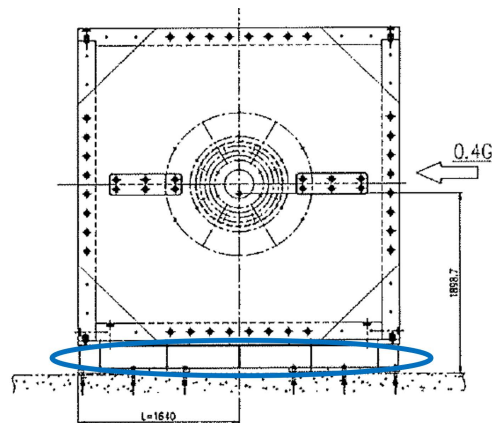Figure 41: Analysis conditions for earthquake resistance of securing bolts during assembly.

Figure 42: Analysis conditions for strength of the base frame.

Table 11: Parameters used for the base frame strength calculation.

Cross section [S]	Quantity	Length (mm)	Thickness (mm)	Total (mm2)
	4	3,800	9	136,800
Weight [M]	Solenoid (kg)	Yoke (kg)	Upper part of the base frame (kg)	Total (kg)
	20,000	115,000	3,414	138,414

Magnetic field measurement

For excitation tests without the return yoke at the manufacturer, we have prepared a magnetic field measurement system as shown in Fig. 43. A 3D Hall probe is mounted on an aluminum frame and scans along the beam axis. The probe is moved one-dimensionally by an ultrasonic motor and a belt. After on-site assembly at the K1.8BR beam line, the magnetic field is measured with the return yoke. We plan to modify the system to allow three-dimensional scanning by remote control, since field measurements are made with the end cap closed.
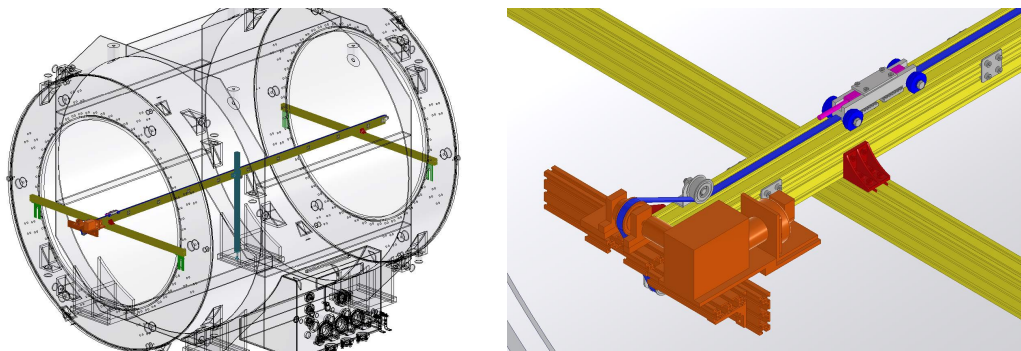
Figure 43: Magnetic field measurement system for excitation tests without the return yoke at the manufacturer, (left) overall view and (right) enlarged view of the drive and Hall probe sections. For on-site measurements, we plan to modify the system to scan in three dimensions by remote control.

Construction schedule

The magnet construction schedule is shown in Fig. 44. The construction of the magnet is a three-year project. In FY2022, we first procured the superconducting wire and constructed the return yoke. We also purchased the GM refrigerators in that fiscal year. In FY2023, we constructed the cold mass and the power supply system with DAQ module. In FY2024, the vacuum vessel will be constructed, followed by its assembly, cooling tests, and excitation tests without the return yoke at the manufacturer. The magnet will then be completed. On-site assembly with the return yoke will be performed in early FY2026. We will then perform an excitation test and magnetic field measurement under actual experimental conditions.

	FY2022				FY2023				FY2024				FY2025				FY2026			
	Q1	Q2	Q3	Q4	Q1	Q2	Q3	Q4	Q1	Q2	Q3	Q4	Q1	Q2	Q3	Q4	Q1	Q2	Q3	Q4
SC Wire		purchase																		
Return Yoke		Construction					stored at KEK													
GM Refrigerators		purchase																		
Cold Mass						Construction														
Power Supply w/ DAQ						Construction														
Vacuum Vessel									Construction											
Assembly																				
Cooling Tests												completion								
Excitation Tests w/o Return Yoke														stored at KEK						
On-site Assembly																				
Excitation Test																				
Magnetic Field Measurement																				

Figure 44: Construction schedule of the magnet.

6.2 Cylindrical Drift Chamber (CDC)

The CDC is a cylindrical wire drift chamber containing 15 layers of anode wires. The design of the new CDC follows that of the existing CDC used for the current CDS at K1.8BR, except that the wire length is about three times longer.

General structure

The structure of the CDC is shown in Fig. 45. The outer radius is 530 mm and the inner radius is 150 mm, with a total length of 2,680 mm. The wire length of the axial layers is 2570 mm, so the angular coverage is $21° < \theta < 159°$ in the polar angle region, corresponding to a solid angle coverage of 93% of 4π.

The CDC consists of two aluminum end plates of 20 mm thickness supported by a 1 mm thick CFRP cylinder of $\phi 303$ mm inner diameter as the inner wall. There is no outer wall, but 50 μm alminized mylar is used to seal the gas volume. The mylar is supported by six CFPR pipes of $\phi 18$ mm outer diameter attached to the outer periphery of the end plates.
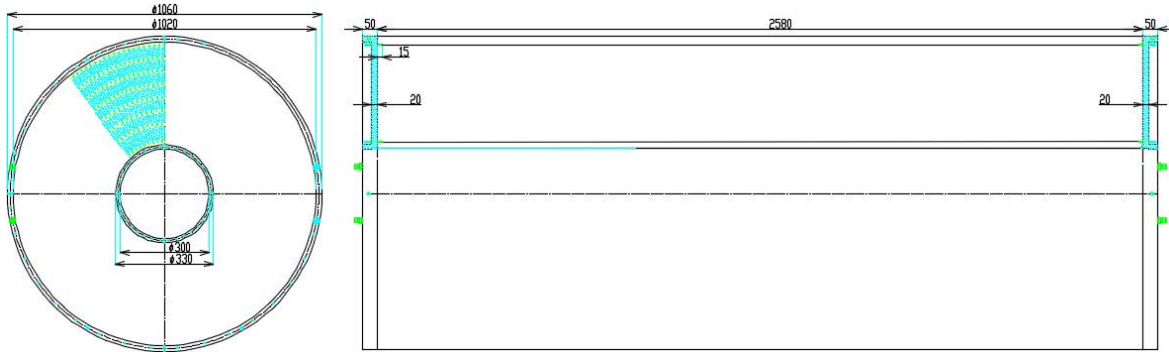
Figure 45: Design of the CDC (all dimensions in mm). The CDC consists of two aluminum end plates and a CFRP cylinder as the inner wall.

Cell structure

The new CDC uses the same cell structure as the existing CDC. The CDC has 15 layers of hexagonal cells with a typical drift length of 9 mm, grouped into 7 super-layers as shown in Fig. 46. Table 12 gives the detailed parameters of the cell configuration. The layers are in the radial range from 190.5 mm (layer #1) to 484.5 mm (layer #15). The 8 stereo layers tilted by about 2.7° are used to obtain longitudinal position information. The number of readout channels is 1,816 and the total number of wires in the CDC is 8,244.
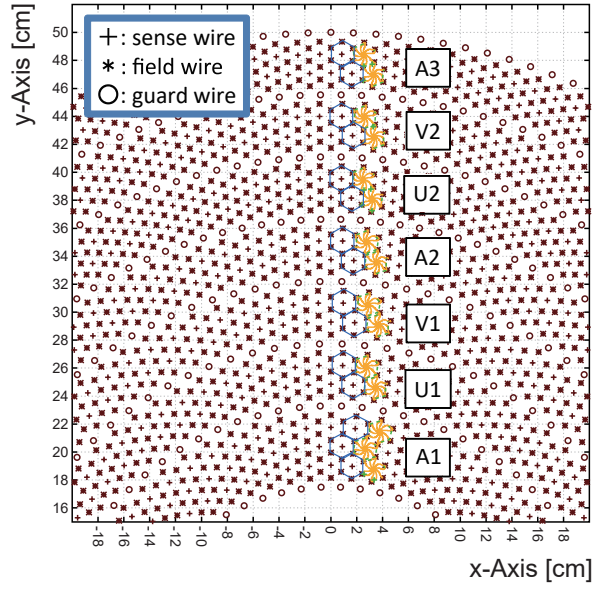
Figure 46: Cell structure of the CDC.

Table 12: Cell configuration of the CDC.

Super-layer	layer	Wire direction	Radius (mm)	Cell width (degree)	Cell width (mm)	Stereo angle (degree)	Signal channels per layer
A1	1	X	190.5		16.7	0	
	2	X'	204.0	5.00	17.8	0	72
	3	X	217.5		19.0	0	
U1	4	U	248.5	4.00	17.3	-2.27	90
	5	U'	262.0		18.3	-2.39	
V1	6	V	293.0	3.60	18.4	2.42	100
	7	V'	306.5		19.3	2.53	
A2	8	X	337.5	3.00	17.7	0	120
	9	X'	351.0		18.4	0	
U2	10	U	382.0	2.40	16.0	-2.82	150
	11	U'	395.5		16.6	-2.92	
V2	12	V	426.5	2.25	16.7	2.96	160
	13	V'	440.0		17.3	3.05	
A3	14	X	471.0	2.00	16.4	0	180
	15	X'	484.5		16.9	0	

Wire configuration

Table 13 summarizes the wire configuration. The CDC uses gold-plated tungsten (Au-W) of 30 μm ϕ for the sense wires and beryllium copper (Be-Cu) of 80 μm ϕ for the field and guard wires. These wires are supported by feedthroughs with a bushing inserted at the end and fixed by soldering. Bushings with 80 and 200 μm ϕ holes are used for the sense and field/guard wires, respectively. To keep the wire sag below 200 μm, the Au-W and Be-Cu wires are tensioned at 70 g and 240 g, respectively. The total load is 1.67 tons with the wire tension of 8,244 wires. Note that the yield point tensions for the Au-W and Be-Cu wires are 150 g and 598 g, respectively, more than twice the tensions used in the CDC.

Table 13: Wire configuration of the CDC.

Wire type	Wire diameter	Wire material	Number of wires	Wire tension
Sense	ϕ30 μm	Au-W	1,816	70 g
Filed	ϕ80 μm	Be-Cu	5,376	240 g
Guard	ϕ80 μm	Be-Cu	1,052	240 g
In total			8,244	1.67 tons

Structural analysis and pretension

The structural calculation with this wire tension is performed as shown in Fig. 47 by the finite element method using the Autodesk Inventor 3D CAD application. The total load of wire tension is applied evenly on two end plates, *i.e.*, half of the total load is applied evenly on the surface of each end plate. The constraint condition is that the inner cylinder is solid and the end plates are fixed to the cylinder. This is because the Young's modulus of the CFRP inner cylinder is 120 GPa in the axial direction and 50 GPa in the r direction, which is strong enough to withstand the total load. As a result, the end plate can deform up to 2.5 mm between the edges of the end plates.

Therefore, the end plates are pretensioned to prevent wire tension changes due to end plate deformation during wire stringing. On the appropriate 6 layers of 67 layers of sense, field, and guard, we install 6 bars on each layer to maintain a certain level of total load evenly during the wire stringing work, *i.e.*, a total of 36 bars are used. We apply a load of 46 kg to make the load on each bar equal. The calculated load transition during the wire stringing is shown in Fig. 48.
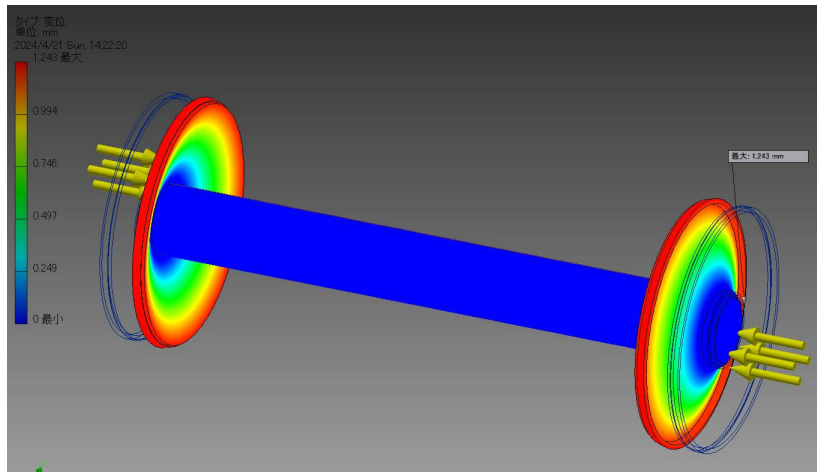
Figure 47: Structural calculation of the CDC. The total wire tension load of 1.67 tons is applied evenly on two end plates. The constraint condition is that the inner cylinder is solid and the end plates are fixed to the cylinder.
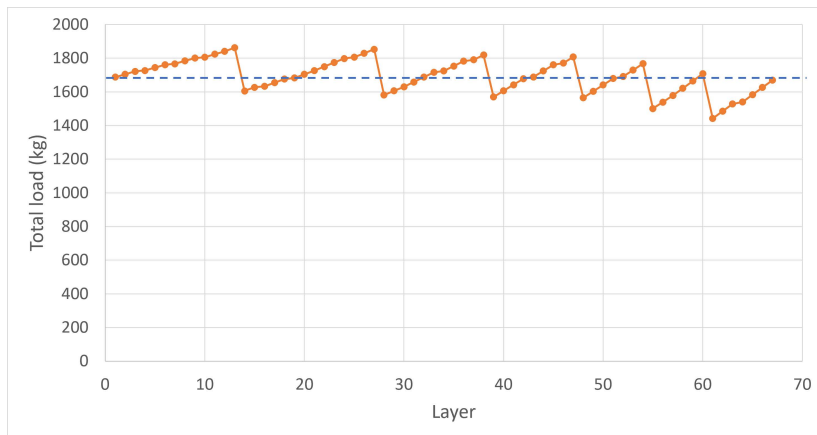

Figure 48: Calculated load transition during wire stringing. As the stringing work progresses from the inside (layer #1), the 280 kg load applied by 6 pretension bars is removed one by one.

Drift gas

The drift gas is a mixture of Argon (90%) - CO_2 (10%) at 1 atm, which is non-flammable, safe to use, inexpensive, and widely used for wire chambers. The gas properties of Ar-CO_2 (90-10), drift velocity and diffusion coefficient versus electric field, evaluated with the Garfield, are shown in Fig. 49. Negative high voltage is applied to the field and guard wires, and the sense wires are kept at ground potential. In December 2023, we conducted a test operation with the existing CDC using Ar-CO_2 (90-10) gas to perform cosmic ray testing without a magnetic field. In operation, we confirmed a sufficient layer efficiency of $\sim 99\%$ comparable to that obtained with the Argon (50%) - Ethane (50%) gas mixture normally used in the existing CDC. Detailed analysis is ongoing, but a position resolution of $\sim 200~\mu$m and a transverse momentum (p_t) resolution of 5.3% $p_t \oplus$ 0.5%/β (σ) are expected, which was achieved with the existing CDC.
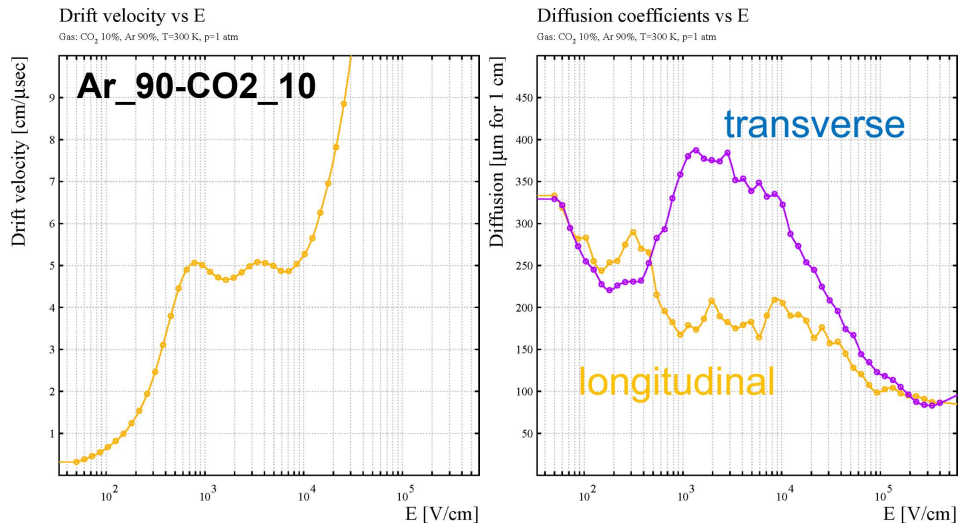
Figure 49: Drift velocity versus electric field (left) and diffusion coefficient versus electric field (right) for Ar-CO2 (90-10) evaluated with the Garfield.

Readout system

The readout electronics of the CDC consists of preamplifiers with ASDs (SONY-CXA3653Q, $\tau = 16$ ns) and HUL multi-hit TDCs, which were used for the existing CDC and we use them as is. For the connection between the feedthroughs and the preamp cards, signal boards are placed directly on the end plates. We make and use new boards of the same design as the existing ones shown in Fig. 50. Through the signal boards, 118 preamp cards are mounted on the CDC.

At the same time, we intend to proceed with studies on the use of preamplifiers using the new ASICs, ASAGI ASD, currently being promoted by the SPADI Alliance.

Figure 50: Existing signal boards placed directly on the end plates of the CDC and its design. We use the same designed boards for the newly constructed CDC.

Construction

Construction of the CDC was started in FY2022 and will be completed in June 2024.

- **FY2022: Production of feedthroughs and purchase of wires.** 17,500 feedthroughs were manufactured by HAYASHI-REPIC CO., LTD. and 7,500 m of goled-plated tungsten wire by LUMA-METALL AB and 28,000 m of beryllium copper wire by NGK INSULATORS, LTD. were purchased.
- **June 2023: Completion of the end plates.** The two end plates shown in Fig. 51 were machined by SEIRITSU CO., LTD.
- **December 2023: Completion of the inner cylinder.** A $\phi 302 \times \phi 304 \times L2580$ CFRP cylinder was manufactured by ASUKA CO., LTD.
- **January 2024: Completion of assembly and start of wire stringing.** The two end plates and the CFRP cylinder were glued together using an assembly jig at HAYASHI-REPIC CO., LTD. After confirming the structural strength, the 36 pretensnioning bars and the six CFRP pipes were installed (Fig. 52). Pretention

Figure 51: CDC endplates machined by SEIRITSU CO., LTD.
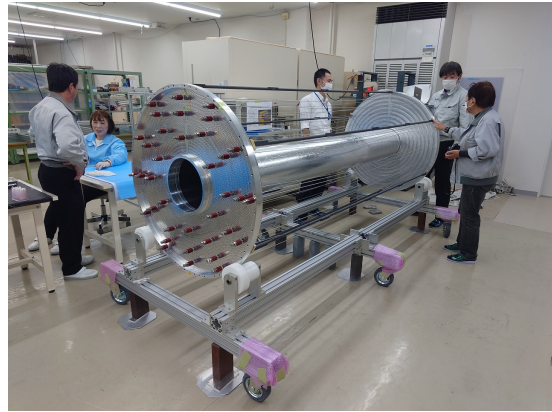
Figure 52: CDC assembly at HAYASHI-REPIC CO., LTD.
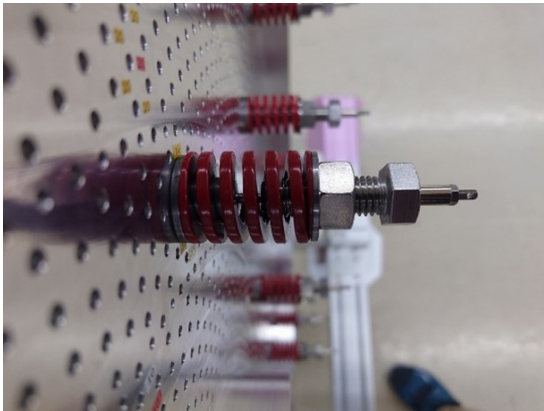
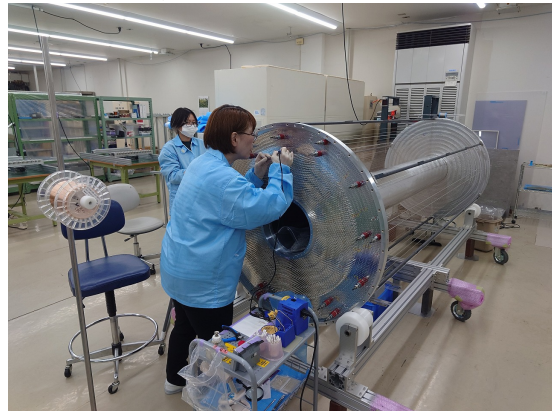Figure 53: Spring coil for application of pretention.

Figure 54: CDC wire stringing work. Two people solder and one person carries the wire between the end plates.

was applied by adjusting the compression length of a spring coil (Fig. 53). Wire stringing work was then started (Fig. 54).

- **May 2024: Completion of wire stringing.** The 8,244 wires were strung through feedthroughs while their tension was measured so that the tension was within 10% of the specified values. As the stringing progresses from the inside, the 280 kg load applied by 6 pretensioning bars was removed one by one as shown in Fig. 48. Transition of the total number of wires strung is shown in Fig. 55. Finally, the tension of all wires was measured again, and the results are summarized in Fig. 56.

- **June 2024: Will be moved to J-PARC.** The gas volume will be sealed with aluminized mylar, then the CDC was completed. The CDC will be moved from the factory to the experiment preparation building at HEF. Cabling and commissioning will take place there.
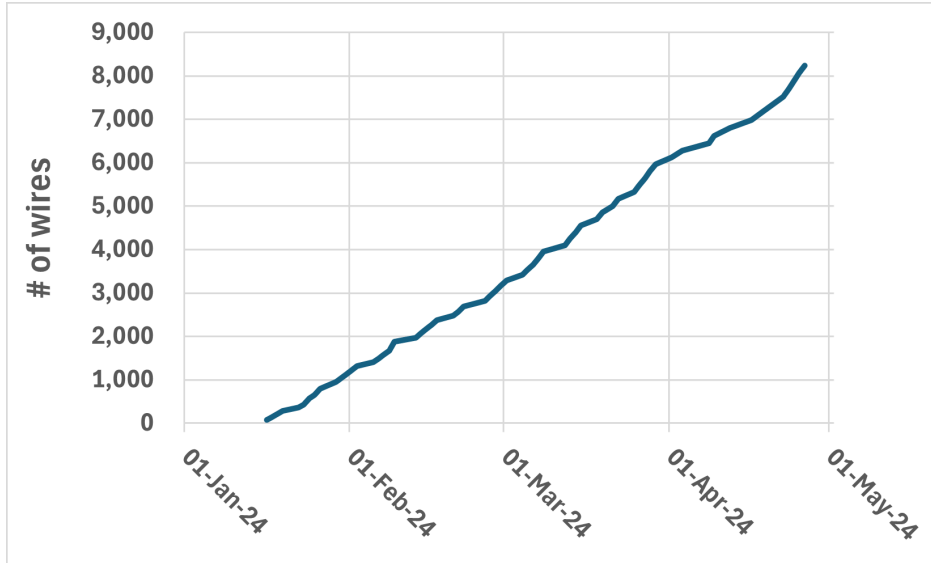
Figure 55: Transition of the total number of wires strung.
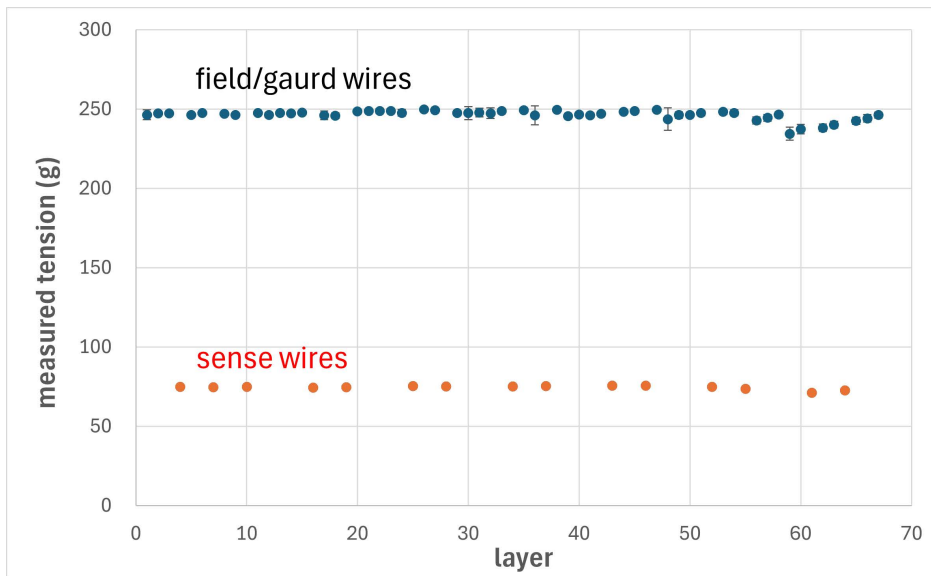
Figure 56: Measured wire tension averaged for each layer. Tension is controlled within 5% of the average.

6.3 Cylindrical Neutron Counter (CNC)

The CNC is an array of segmented plastic scintillation counters used for neutron detection. Charged particle identification and decay particle triggering are also performed on the first layer of the CNC. The CNC will be used for a polarimeter scatter in the spin/parity determination of kaonic nuclei proposed as the P89 experiment.

General structure

The CNC has a total thickness of 12 cm and a length of 3.0 m, which is divided into two layers as shown in Fig. 57. The expected neutron detection efficiency is $12\% \sim 36\%$ depending on the neutron momentum. The first layer is located at a radius of 548 mm from the beam axis and covers a polar angle range of 21 to 159 degrees. The coverage is the same as the CDC, *i.e.*, a solid angle coverage of 93% of 4π. The first layer of the NC is also used for charged particle identification as a hodoscope counter. The second layer is located at 780 mm, of which the solid angle coverage is $29° < \theta < 151°$ in the polar angle region, corresponding to 87% of 4π coverage. The wide gap between the scintillators is prepared for the installation of polarimeter trackers: between the first and second layers of the CNC and between the second layer and the inner wall of the magnet.
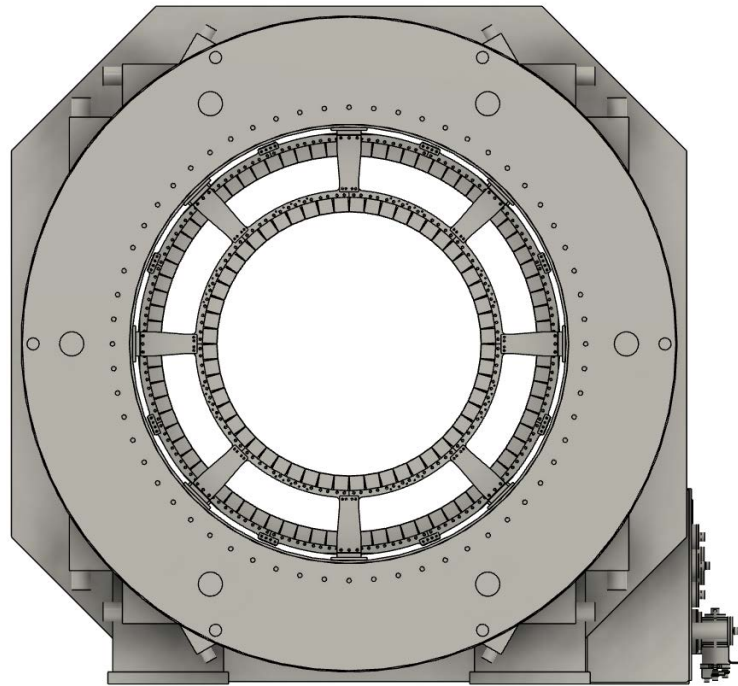
Figure 57: Schematic drawing of the CNC. The CNC consists of 56 and 80 modules in the first and second layer, respectively.

Segmented module and its readout

The CNC consists of 56 and 80 modules in the first and second layers, respectively, whose scintillators are made of Eljen EJ-200. All scintillators are the same size, 60 mm square and 3 m long, so they can be easily rearranged for experiments. In the first layer, the scintillation light is transferred directly to a pair of Hamamatsu R7761 19-dynode fine mesh photomultipliers (FM-PMTs) with a diameter of 1.5 inches (H8409). These FM-PMTs are the same type used in the Cylindrical Detector Hodoscope (CDH) of the existing CDS, where we used the 72 PMTs. We use the 112 FM-PMTs we currently have in stock, including those used in the CDH. The second layer uses a pair of silicon photomultiplier arrays for readout because the 1.5 inch FM-PMT is discontinued and no longer available. We use a Hamamatsu MPPC (Multi-Pixel Photon Counter) array with 4×4 channels consisting of 6×6 mm^2 photo sensors (S13361-6050AE-04). The MPPC array is read out with a parallel connection combined with a hybrid connection as shown in Fig. 58 using a single channel readout amplifier. The amplifier consists of two RF amplifiers (HPMA-0385) and a pole-zero cancellation circuit whose block diagram is shown in Fig. 59. As for the QDC and TDC, we use the same readout system currently used for the CDH, *i.e.*, CAEN V792 QDC and HUL HR-TDC, with some additions.
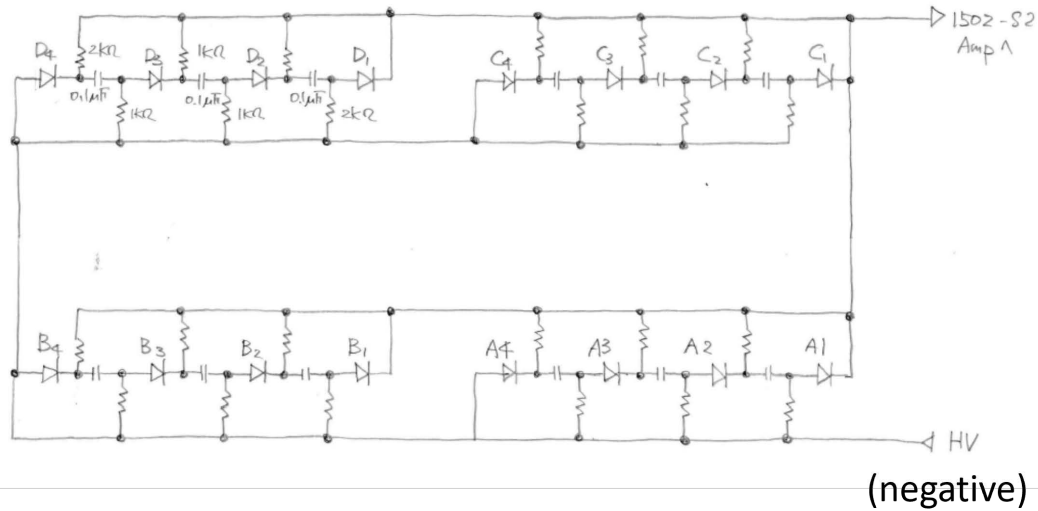
Figure 58: Readout scheme of the MPPC array using a parallel connection combined with a hybrid connection.
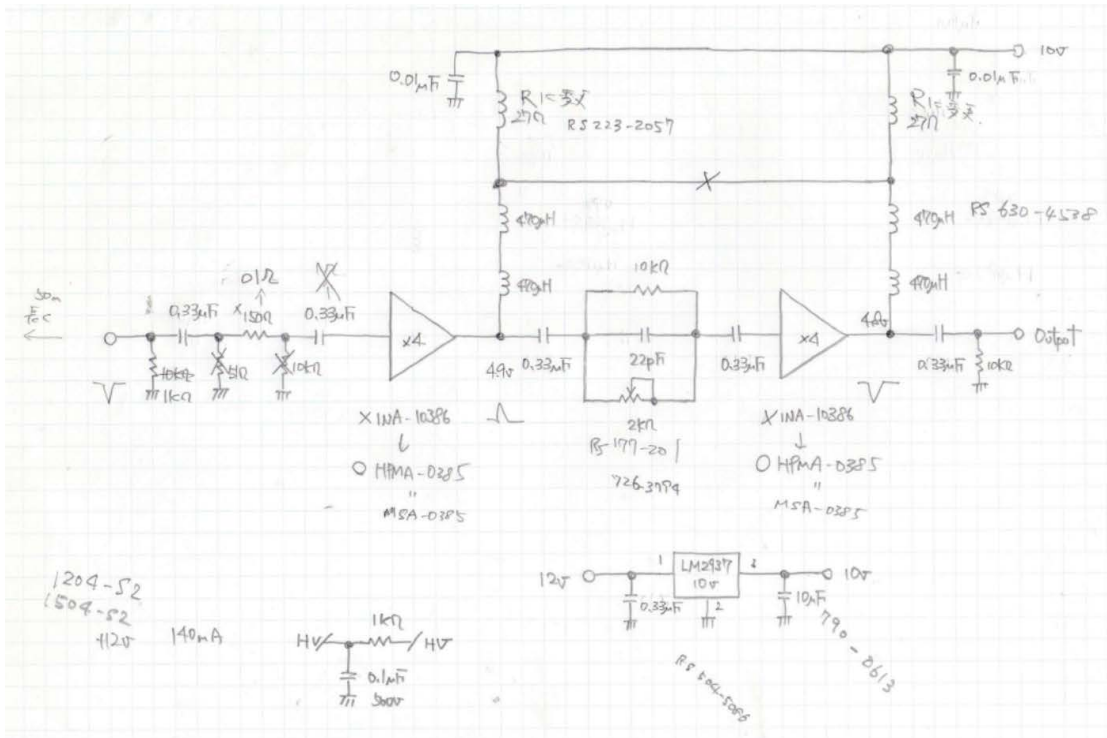
Figure 59: Block diagram of the MPPC amplifier.

Operation in the magnetic field

The CNC is operated in the 0.7 T magnetic field with a typical PMT gain of $\sim 10^6$, as in the case of the existing CDS. Figure 60 shows a comparison of the magnitude and direction of the calculated magnetic field between the new CDS and the existing CDS. The magnetic field direction at the location of the FM-PMT is approximately parallel to the photomultiplier axis in both cases. At the existing CDS, the FM-PMT gain of approximately 10^6 was safely achieved under 0.7 T operation, so the FM-PMT is expected to work well in the new CDS.

New CDS

Existing CDS

1.0T

0.7T
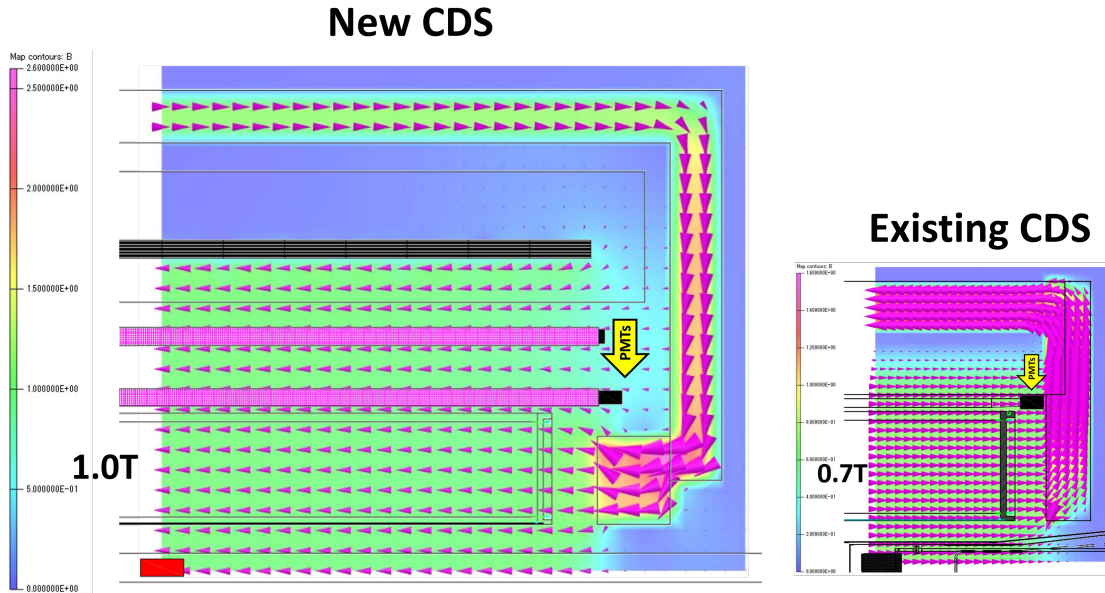
Figure 60: Magnitude and direction of the calculated magnetic field of (left) the new CDS and (right) the existing CDS.

R&D with prototypes

Using the first prototype modules with $130 \times 50 \times 2,600$ mm scintillator, we performed a test experiment at ELPH in 2022-23. We obtained a time resolution of approximately 110 ps independent of the longitudinal position as shown in Fig. 62, which meets a minimum requirement of less than 150 ps. To further improve the time resolution, we have now prepared the second prototype modules with a narrower scintillator width closer to the current CNC design. The sizes of the modules are $50 \times 50 \times 2,600$ mm and $50 \times 60 \times 2,600$ mm, which were fabricated from the first prototype. We will test the prototype modules with a 1 GeV/c beam at K1.8BR in May-June 2024 to verify the time resolution. Further detailed studies, such as the position dependence study, are planned at J-PARC and/or ELPH in 2024. In addition, an R&D study of the MPPC amplifier with temperature control circuit is underway, including the design of the board shape to be mounted at both ends of the CNC.

Construction schedule

The scintillators will be purchased in FY2024. The R&D study of the amplifier with temperature control circuit will also be completed and ready for mass production in FY2024. MPPC arrays will be purchased and amplifier boards will be manufactured in early FY2025. Assembly and commissioning with cosmic rays will follow.

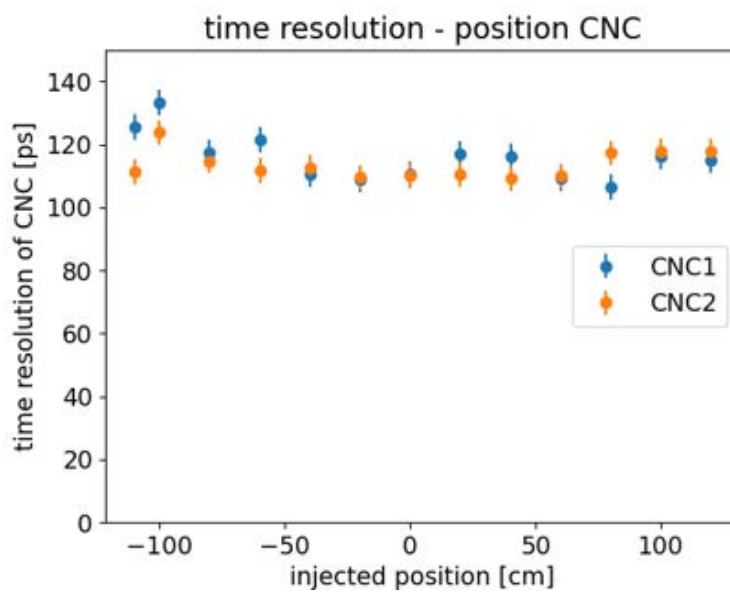Figure 61:   First prototype module of the CNC.

Figure 62:   Longitudinal position dependence of the time resolution of the first proto-
type CNC modules, obtained in a test experiment at ELPH in 2022-23.

6.4 Vertex Fiber Tracker (VFT)

High-resolution vertex determination is essential to discriminate between the signals and backgrounds with event topology such as the distance of closest approach method. With CDC alone, the vertex resolution in the beam direction (z-direction) is ~ 1 cm, while that in the radius direction (r-direction) is a few mm. This is due to the small tilt angle of the stereo layers, which is limited by the wire layout. By introducing the VFT, the vertex resolution in the beam direction is expected to be improved to a few mm by combining the CDC tracking information. The momentum resolution is also expected to improve with the introduction of the VFT, as shown in Fig. 63.
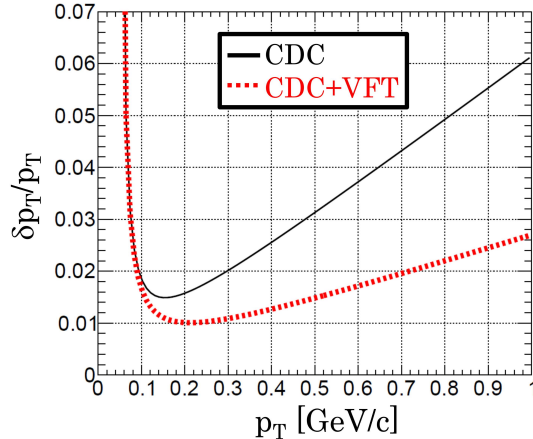
Figure 63: Comparison of the transverse momentum resolution (σ) between the CDC alone and the CDC+VFT.

The VFT is mounted on the outer wall of the target chamber ($r \sim 55$ mm) and covers a polar angle range from 15 to 165 degrees, corresponding to a solid angle coverage of 97% of 4π. We use 4 layers of 1 mm ϕ scintillating fibers in the $UU'VV'$ configuration. In the U and V layers, the fibers are tilted by ± 45 degrees. The total number of readout channels is 896 ($= 224 \times 4$). For readout, CIRASAME modules developed for the fiber tracker system in the E50 experiment will be used.

In FY2023, a prototype of the VFT was installed on the existing CDS as shown in Fig. 64 to be used as a vertex tracker for the E73 experiment, the direct measurement of hypertriton lifetime. During the beam tuning of the T98 phase 1 experiment in June 2023, the VFT was put into operation. In the preliminary studies, the vertex resolution in the beam direction was improved to 1.7 ± 0.2 mm with a combination of the CDC tracking information, from 5 ± 2 mm with the CDC tracking only as shown in Fig. 65 [45]. We will use almost the same system for the new CDS.
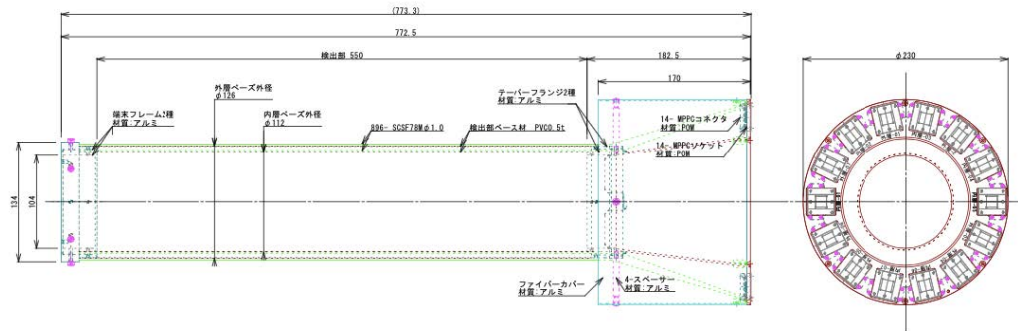
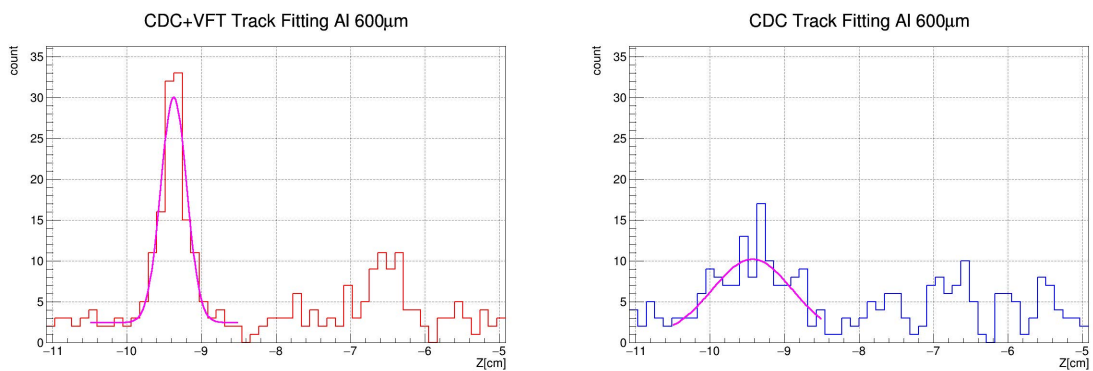Figure 64: Schematic drawing (left) and photo in June 2023 (right) of the VFT [45].

Figure 65: Fitting to the peak corresponding to the 0.6 mm thick aluminum target chamber window [45]. The vertex point obtained using the beam and CDC+VFT tracks is shown on the left, and that obtained using the beam and CDC tracks is shown on the right.

6.5   Support Structure of the CDS

The design of a support structure for the internal detector of the CDS is important for safe installation and easy maintenance of the detector. In particular, it is necessary to install the detector accurately so that the detector is not distorted by its own weight. Due to space limitations upstream of the K1.8BR region, the detector should be installed from downstream of the beam.

General structure

To achieve these goals, a support structure of the CNC and CDC is built directly into the inner wall of the magnet; pillars are mounted on the inner wall to which the CNC and CDC are attached. Since the total weight of the CDC and CNC including the support structure is approximately 1.5 tons, the pillar structure is designed to be strong. A design of the support structure for the CDC and CNC is shown in Fig. 66. The pillars are mounted on the inner wall of the magnet first, then the CNC is installed, followed by the CDC installation. The CNC is installed using three ring support structures of upstream, middle, and downstream sections which are mounted on the pillars. Each CNC module is mounted on the ring structures using support jigs and thin stainless steel bands. The CDC is mounted on the pillars at the upstream and downstream sections.
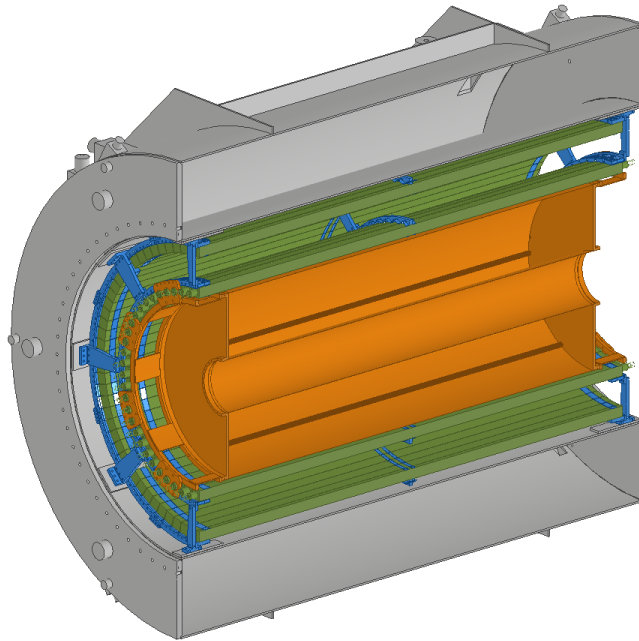

Figure 66:   Schematic drawing of the support structure of the CDS.

Detector installation method

For efficient and safe construction, CNC assembly is performed in 90-degree increments from the 90-degree top, left, and right sections. The 90-degree bottom section is installed last. Three-quarters of the second layer is installed first, and then three-quarters of the first layer is installed. Finally, the remaining 90-degree bottom sections of the second and first layers are installed in sequence.

After the CNC installation, the CDC is installed by inserting a long frame bar into the center of the CDC and magnet, and aligning the center position with the beam height. The long frame bar is at least twice the length of the CDC. The CDC is manually rolled into the magnet along this bar, and finally the CDC is fixed to the pillars from both end plates. This CDC installation method using a long bar has already been adopted for the existing CDS, so we will follow this method for the new CDS. A photo of the existing CDC installation is shown in Fig. 67 for reference. Therefore, a space equivalent to the installation area of the magnet is required downstream of the magnet to prepare and install the CDC by rolling it in and out of the magnet as shown in Fig. 68.
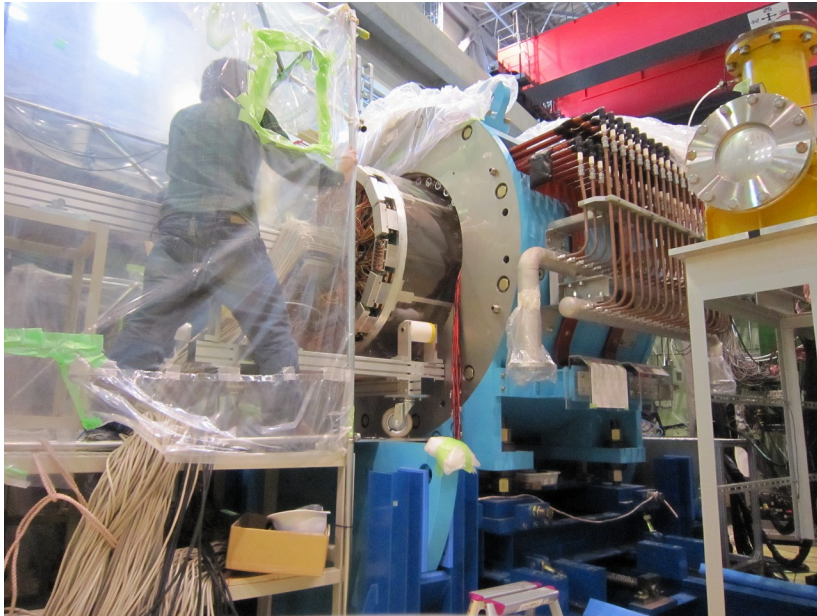

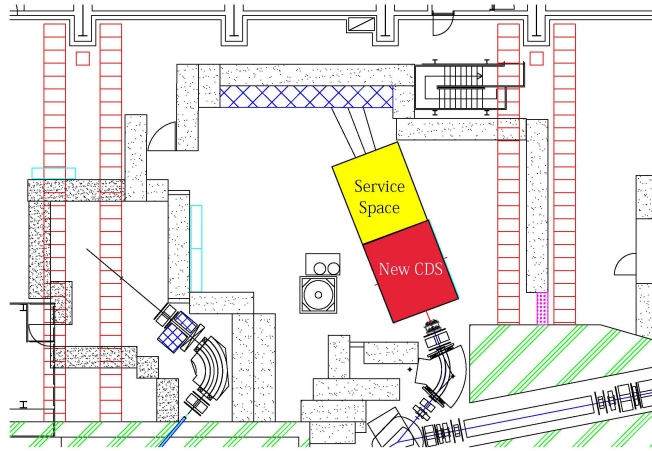Figure 67: Photo of the existing CDC installation.

Figure 68: New CDS and a service space on the new K1.8BR experimental area.

Cable support

The cable support structure is built inside the return yoke. The cables for the CDC and CNC are fixed to the structure, and the cables are pulled out through the holes in the four corners of the return yoke shown in Fig. 69. Cable handling when rolling in/out of the CDC can be done outside the return yoke.
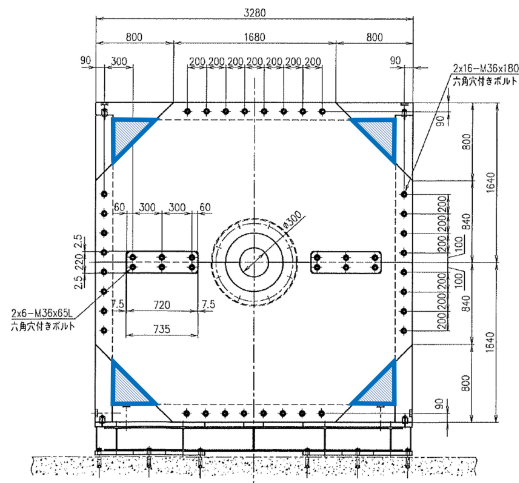

Figure 69: Holes in the four corners of the return yoke (blue hatched). The cables for the CDC and CNC are pulled out through these holes.

Structural analysis

Structural calculations are performed to determine if the support structure can support the weight of the CDC and CNC. The stresses and displacements are calculated by the finite element method using the Autodesk Inventor 3D CAD application. The calculation uses PMMA, A5083, and SUS304 as the materials for the scintillator, aluminum frame, and the inner cylinder of the magnet, respectively. Here, the parts are bonded together. A gravity of 2 G is applied from the vertical direction, and the constraint condition is the end face of the inner cylinder. The structural calculation model is shown in Fig. 70.

Figure 71 and 72 show the calculated results. In this configuration of the support structure, the maximum stress is less than 30 MPa at any point, *i.e.*, no excessive stress is applied to the structure. The sag of the sintillators is about 1 mm, which is sufficient accuracy of the detector integration.

Figure 70: Structural calculation model. The constraint condition is the end face of the inner cylinder of the magnet, and the parts are glued together. A gravity of 2 G is applied from the vertical direction.
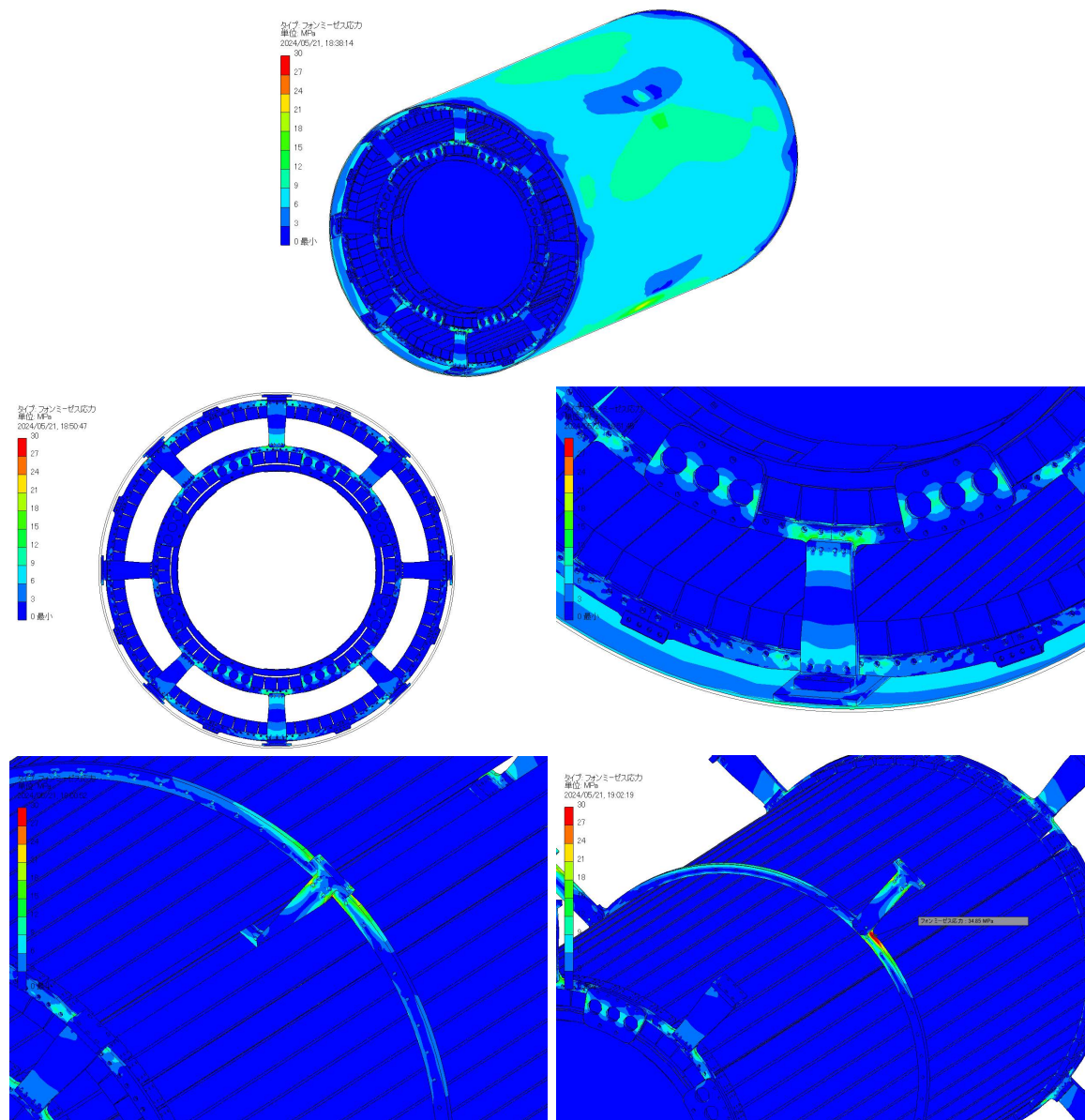
Figure 71: Results of stress distributions: overall (top), support frame (center left), base part of the inner cylinder (center right), support frame at the CNC outer and inner layers at center of inner cylinder (bottom left and right).
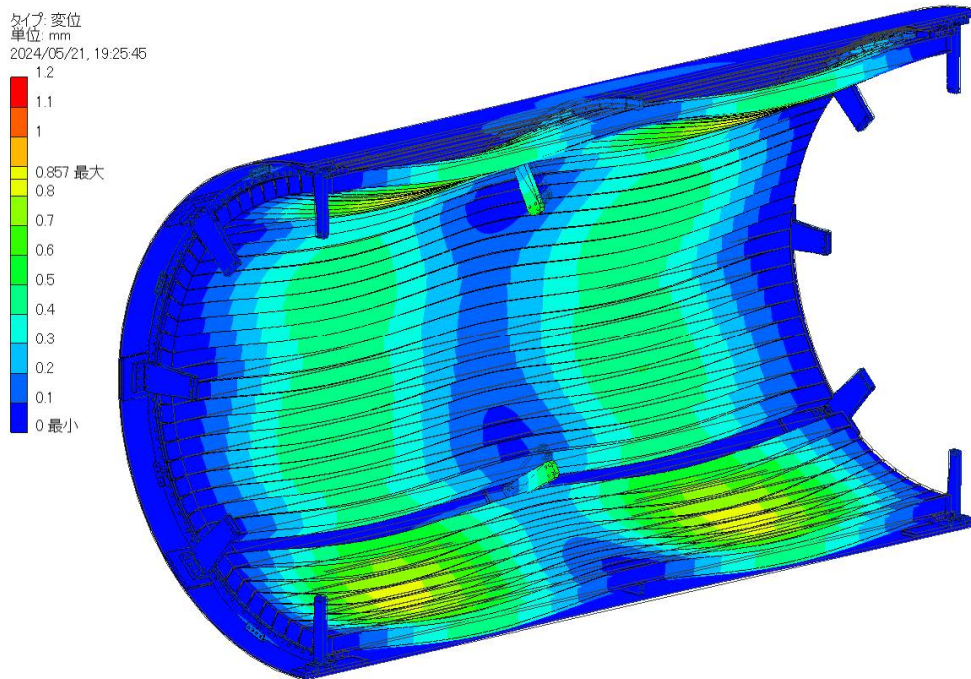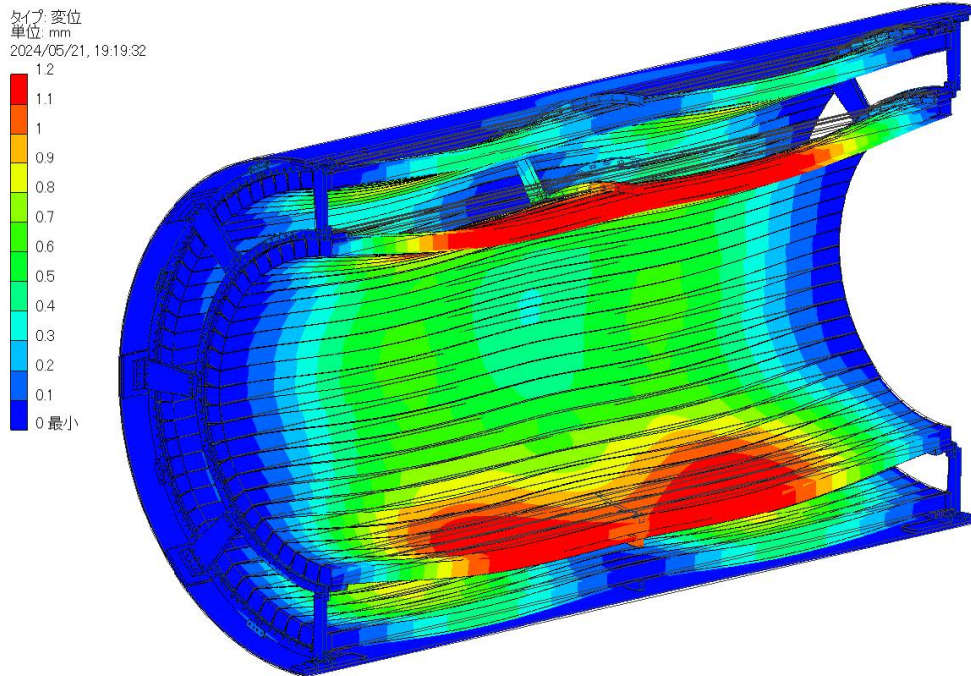
Figure 72: Results of the displacements: the CNC inner layer (top) and the outer layer (bottom).

7 Trigger and DAQ systems

A dedicated hardware trigger is developed to meet the experimental requirements. The kaon beam trigger is constructed in the same way as in the previous experiments on the K1.8BR beam line. The elementary beam trigger is constructed using coincidence signals from the beam line counters (BHT*T0), and the kaon beam trigger is selected from the beam trigger using the kaon identification counter ($\overline{\text{AC}}$).

To select an event associated with the $K^- ppn$ decay, we use the simplest charged-multiplicity trigger implemented at the hardware level with the first layer of the CNC (fCNC). For the main trigger of E80, the fCNC three-hit event (fCNC_3) is used to measure K^- ^{4}He $\rightarrow$ "$K^- ppn$" $n \rightarrow \Lambda dn \rightarrow \pi^- pdn$; three charged particles ($\pi^- pd$) are required in the CDS to reconstruct the "$K^- ppn$" $\rightarrow \Lambda d$ decay. This trigger also covers the detection of the K^- ^{4}He $\rightarrow$ "$K^- ppn$" $n \rightarrow \Lambda pnn \rightarrow \pi^- ppnn$ event.

We use the HDDAQ framework as the online data acquisition system, whose maximum accumulation rate has been confirmed to reach $\sim$ 10 k events per spill with more than 90% DAQ efficiency. In the E80 experiment, the expected trigger rate of the main trigger, fCHC_3, is $\sim$ 10 k per spill, taking into account the results of the previous experiments as summarized in Table 14. The trigger rate is thus controllable.

Table 14: Measured and estimated trigger rate. The unit is events per spill. The trigger rate of E80 with the CDS (Kaon*fCNC_n) is estimated using the E73 results in April 2024 by taking into account the increased beam power and solid angle: estimated trigger rate = E73(81kW,4.2s) $\times$ 90kW/81kW $\times$ 1.4 $\times$ (93%/59%)$^{\text{fCNC\_n}}$.

	81 kW (E73, Run91)	90 kW (E80)
Beam (BHT*T0)	1,600 k	2,500 k
Pion_all (Beam*AC)	1,100 k	1,700 k
Kaon_all (Beam*$\overline{\text{AC}}$)	490 k	760 k
Kaon (Beam*$\overline{\text{AC}}$*DEF)	250 k	390 k
Kaon*CDH_1[fCNC_1]	17k	42k
Kaon*CDH_2[fCNC_2]	5.9k	23k
Kaon*CDH_3[fCNC_3]	1.9k	12k

8 Acknowledgments

References

[1] M. Iwasaki *et al.* *Phys. Rev. Lett.* **78** (1997) 3067.

[2] G. Beer *et al.* *Phys. Rev. Lett.* **94** (2005) 212302.

[3] M. Bazzi *et al.* *Phys. Lett.* **B704** (2011) 113.

[4] A. D. Martin *Nucl. Phys.* **B179** (1981) 33.

[5] Y. Nogami *Phys. Lett.* **7** (1963) 288.

[6] Y. Akaishi and T. Yamazaki *Phys. Rev.* **C65** (2002) 044005.

[7] T. Yamazaki and Y. Akaishi *Phys. Lett.* **B535** (2002) 70.

[8] N. V. Shevchenko, A. Gal, and J. Mares *Phys. Rev. Lett.* **98** (2007) 082301.

[9] N. V. Shevchenko, A. Gal, J. Mares, and J. Révai *Phys. Rev.* **C76** (2007) 044004.

[10] Y. Ikeda and T. Sato *Phys. Rev.* **C76** (2007) 035203.

[11] A. Doté, T. Hyodo, and W. Weise *Nucl. Phys.* **A804** (2008) 197.

[12] Y. Ikeda and T. Sato *Phys. Rev.* **C79** (2009) 035201.

[13] S. Wycech and A. M. Green *Phys. Rev.* **C79** (2009) 014001.

[14] A. Doté, T. Hyodo, and W. Weise *Phys. Rev.* **C79** (2009) 014003.

[15] Y. Ikeda, H. Kamano, and T. Sato *Prog. Theor. Phys.* **124** (2010) 533–539.

[16] N. Barnea, A. Gal, and E. Z. Liverts *Phys. Lett.* **B712** (2012) 132.

[17] M. Bayar and E. Oset *Phys. Rev.* **C88** (2013) 044003.

[18] S. Maeda, Y. Akaishi, and T. Yamazaki *Proc. Jpn. Acad.* **B89** (2013) 418.

[19] J. Révai and N. V. Shevchenko *Phys. Rev.* **C90** (2014) 034004.

[20] A. Doté, T. Inoue, and T. Myo *Prog. Theor. Exp. Phys.* **2015** (2015) 043D02.

[21] T. Sekihara, E. Oset, and A. Ramos *Prog. Theor. Exp. Phys.* **2016** (2016) 123D03.

[22] S. Ohnishi, W. Horiuchi, T. Hoshino, K. Miyahara, and T. Hyodo *Phys. Rev.* **C95** (2017) 065202.

[23] A. Doté, T. Inoue, and T. Myo *Phys. Rev.* **C95** (2017) 062201.

[24] A. Doté, T. Inoue, and T. Myo *Phys. Lett.* **B784** (2018) 405.

[25] M. Agnello *et al.* *Phys. Rev. Lett.* **94** (2005) 212303.

[26] T. Yamazaki *et al.* *Phys. Rev. Lett.* **104** (2010) 132502.

[27] Y. Ichikawa *et al.* *Prog. Theor. Exp. Phys.* **2015** no. 2, (2015) 021D01.

[28] O. Vázquez Doce *et al.* *Phys. Lett.* **B758** (2016) 134.

[29] R. Del Grande *et al.* *Eur. Phys. J.* **C79** (2019) 190.

[30] G. Agakishiev *et al.* *Phys. Lett.* **B742** (2015) 242.

[31] A. O. Tokiyasu *et al.* *Phys. Lett.* **B728** (2014) 616.

[32] T. Hashimoto *et al.* *Prog. Theor. Exp. Phys.* **2015** (2015) 061D01.

[33] Y. Sada *et al.* *Prog. Theor. Exp. Phys.* **2016** (2016) 051D01.

[34] S. Ajimura *et al.* *Phys. Lett.* **B789** (2019) 620.

[35] T. Yamaga *et al.* *Phys. Rev. C* **102** (2020) 044002.

[36] Letter of Intent for J-PARC, 2009, "Double Anti-kaon Production in Nuclei by Stopped Anti-proton Annihilation" *http: // j-parc. jp/ researcher/ Hadron/ en/ Proposal_ e. html* .

[37] Y. Kanada-En'yo *Eur. Phys. J. A* **57** (2021) 185.

[38] T. Kishimoto *Phys. Rev. Lett.* **83** (1999) 4701.

[39] Proposal for J-PARC, 2021, "Proposal for the E80 Phase-I Experiment: Investigation of the $\bar{K}NNN$ Bound State Focusing on the Λd Decay *http: // j-parc. jp/ researcher/ Hadron/ en/ Proposal_ e. html* .

[40] J. Allison *et al.* *Nucl. Instrum. Meth.* **A835** (2016) 186.

[41] Y. Yamaga *et al.* `arXiv:2404.01773 [nucl-ex]`.

[42] O. Sasaki and M. Yoshida *IEEE Transactions on Nuclear Science* **46** (1999) 1871.

[43] M. Yoshida *et al. IEEE Transactions on Applied Superconductivity* **21** (2011) 1752.

[44] *AIJ Design Standard for Steel Structures - Based on Allowable Stress Concept.* Architectural Institute of Japan, 2007.

[45] E. Hodota, *Performance evaluation of the Vertex Fiber Tracker for precise measurement of Kaonic nuclei at J-PARC.* Master thesis, Tohoku University, 2024.